AMERICAN UNIVERSITY OF BEIRUT

THE FLOW DYNAMICS ABOUT A CYLINDRICAL CACTUS PLANT MODEL IN CROSS WIND

by
ADNAN MILAD EL MAKDAH

A thesis
submitted in partial fulfillment of the requirements
for the degree of Master of Mechanical Engineering
to the Department of Mechanical Engineering
of the Faculty of Engineering and Architecture
at the American University of Beirut

Beirut, Lebanon
September 2012

AMERICAN UNIVERSITY OF BEIRUT

THE FLOW DYNAMICS ABOUT A CYLINDRICAL CACTUS PLANT MODEL IN CROSS WIND

by

ADNAN MILAD EL MAKDAH

Approved by:

Dr. Ghanem Oweis, Assistant Professor Department of Mechanical Engineering	Advisor
Dr. Nesreene Ghaddar, Professor Department of Mechanical Engineering	Member of Committee
Dr. Issam Lakkis, Associate Professor Department of Mechanical Engineering	Member of Committee

Date of thesis defense: September 21, 2012

AMERICAN UNIVERSITY OF BEIRUT

THESIS RELEASE FORM

I, Adnan Milad El Makdah

☐ Authorize the American University of Beirut to supply copies of my thesis to libraries or individuals upon request.

☐ Do not authorize the American University of Beirut to supply copies of my thesis to libraries or individuals for a period of two years starting with the date of the thesis defense.

_____

Signature

_____

Date

ACKNOWLEDGMENTS

I would like to thank all the people that supported and helped me in the past two years. Without them, I wouldn't finish this thesis.

I thank my advisor Dr. Ghanem Oweis for his continuous support and guiding me throughout my master. Moreover, I want to extend my gratitude to the committee members: Dr. Nesreene Ghaddar and Dr. Issam Lakkis.

Thanks to all my friends and colleagues in AUB. Thanks to my friends in the fluids lab Lory Kevorkian and Moath Al Qraini.

Lastly and most importantly, thanks to my entire family who was beside me every minute of my study years. My father Milad, and my mother Hala, thank you for raising, supporting and teaching me. To you I dedicate my thesis.

AN ABSTRACT OF THE THESIS OF

Adnan Milad El Makdah for Master of Engineering
Major: Mechanical Engineering

Title: The Flow Dynamics about a Cylindrical Cactus Plant Model in Cross Wind

Researchers were in many occasions inspired from the biology field in order to improve engineering systems. Cactus trees are long cylindrical plants with longitudinal grooves. They have survived the harsh dessert environment resisting the strong sand storms despite their weak rooting system. Therefore, they are thought to have an aerodynamic superiority on their counterpart circular cylinders. Particle Imaging Velocimetry (PIV) was used to study the flow in the wake and the grooves of a cactus shaped cylinder model. Experiments were done in an open loop L-shaped wind tunnel at flows of high Reynolds numbers of 50×10^3 to 200×10^3 which mimics the strong wind storms. Detailed mean and instantaneous flow analysis were done. Moreover, vorticity analysis was done on the shear layer of the grooves and the immediate wake of the cactus in order to understand the vortex shedding and their interactions. Our results showed an improved aerodynamic behavior for the cactus as its wake showed lower stream wise turbulent intensity than its counterpart circular cylinder. Furthermore, the role of the grooves was identified in improving the vortex shedding. The spikes of the cactus act as a vortex generator that help in reducing the shear and friction forces and lubricate the flow around the cactus cylinder.

CONTENTS

ILLUSTRATIONS

Figure Page

CHAPTER I

INTRODUCTION

Cactus Trees are tall cylindrical plants with longitudinal grooves. Theycan withstand the harsh environment of the desert, and survived the high wind of many sand storms despite the fact that they have weak rooting system. Therefore, cactus plants have special aerodynamic properties that helped them to be naturally selected to survive the deserts according to Darwin's theory. In this thesis, the aerodynamic behavior of cactus plants will be experimentally investigated specifying the effects of the grooves on the flow against the cactus.

A. Bluff Bodies and Vortex Shedding

A bluff body is defined as a body that has a broad, flattened front usually being perpendicular to the flow such as cylinders and spheres. The flow against bluff bodies is characterized by the early separation of the boundary layer creating unsteady wakes in general, which in consequence will cause structural vibrations and noise. Therefore, bluff bodies flow is an important problem in various engineering applications. Flows against buildings, towers, bridges and vehicles are some examples of the flow behind bluff bodies. Extensive studies and investigations were done on external flows in order to understand the interaction of the flowing fluid with the body, and to understand the lift and drag forces that are exerted on the body by the flow [1].

The physics behind the separated bluff bodies flow can be typified by the flow behind a two dimensional circular cylinder. The problem of the circular cylinder flow

possess the complexities of shear layer separation, vortex rolling up and interactions, the aerodynamic flow loads such as drag and lift forces, and turbulence fluctuations in general [1]. Therefore, many experimental and numerical studies were done on the cylinders' flows throughout the last decades. Strouhal (1878) was the first one to be able to correlate the frequency of the shedding with the flow speed. Moreover, the mechanisms and changes in the structure of the flow, the drag coefficient C_D, pressure coefficient C_P, and the vortex shedding frequency - designated by the dimensionless Strouhal number (St) - were identified with respect to Reynolds number (Re) for the circular cylinder – which is a dimensionless number that represents the ratio of the inertial forces to the viscous forces of the flowing fluids ($Re = \frac{\rho UD}{\mu}$; whereρ,U,D, and μ are the fluid density, upstream velocity, Characteristic model diameter, and fluid viscosity respectively). For Re<250, the shedding behind the cylinder is laminar and two dimensional. However, as Re increases the shedding flow starts to be three dimensional; moreover, as Re increases further Re>1000, the vortices shedding becomes laminar. The boundary layer stays laminar until Re of nearly2.5×10^5. The behavior of the circular wake versus Re number is shown in Figure 1.

One of the important phenomena of the separated bluff bodies flow is the vortex shedding. It is the formation and the interaction of periodic alternating clockwise and counterclockwise vortices with each other in the near wake of the bluff body. The shedding starts to form at the critical Re number of 49 [1], and it causes structural vibrations that can lead to complete structural failure if the frequency of the shedding couples with the natural resonance frequency of the bluff body. According to Gerrard (1966), the interaction between the separated upper and lower shear layers plays an important role in the shedding. When the upper shear layer dominates the lower shear

layer in the vortex shedding formation region and it rolls into a vortex of increasing strength, the lower shear layer starts to roll into a vortex of swirling direction opposite to that of the upper shear layer and of equal strength.

The strength and frequency of the vortex shedding are highly correlated to the drag and pressure coefficients. Therefore, researchers investigated various methods to control the shedding in order to alleviate its effect on the body.

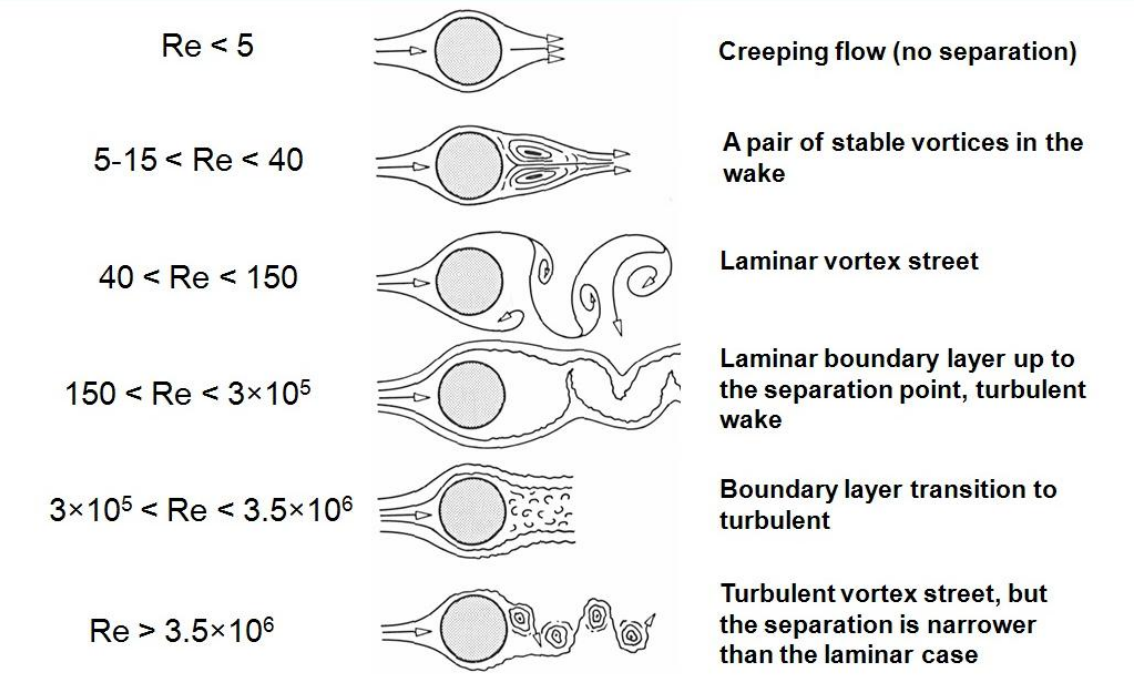

Figure 1: Circular cylinder wake versus Reynolds number

B. Literature Review

The flows behind bluff bodies were extensively studied in order to understand the shedding behind them. Understanding the flow will allow the possibility of altering it to reduce the drag force. The flow behind a circular cylinder was of special interest for researchers for it typifies the separated flow of bluff bodies. Roshko (1955) [2] was

the first one who measured the period of the Karman vortex shedding behind a bluff body. Afterwards, many researchers investigated the near wake flow structure and its impact on the body as reported in the reviews by Berger & Wille (1972) [3], Lin & Pao (1979) [4], Bearman (1984) [5], Oertel (1990) [6], Griffin & Hall (1991) [7], Coutanceau & Defaye (1991) [8], and Williamson (1996, 2004) [9, 10]. J. H. Gerrard (1961) [11] determined experimentally the oscillating lift and drag forces exerted on a circular cylinder resulted from the vortex shedding near the wake. He did so by measuring the surface pressure fluctuations. He found that the oscillations in the drag and lift forces increase as the Reynolds number increases. Williamson (1996, 2004) explained in his review the dynamics of vortex shedding and how it is affected by Reynolds number in addition to the geometry and the shape of the bluff body. He also explained the transition of the boundary layer from laminar to complete turbulent layer and reported the vortices behavior in the near wake. Bearman & Zdravkovich (1977) [12] studied the vortex shedding behind a circular cylinder placed at different heights from a plane boundary. They measured the pressure distributions around both the circular cylinder and the plane boundary, and they found that vortex shedding was suppressed for all gaps that are less than 30% of the cylinder's diameter.

Understanding the phenomenon of vortex shedding, many researchers suggested different methods to control the near wake flow in order to suppress the shedding, or at least to alleviate its effects on the bluff body in terms of lift and drag forces. These methods can be categorized into two control types: Active and passive. Active control methods need external forces to alter the flow, which in consequence requires an energy input. Some examples are applying a rotary force on the bluff body (Baek & Sung 1998 [13]; Choi et al. 2002 [14]), applying an electromagnetic force on the flow (Artana et al. 2003 [15], Kim &

Lee 2000 [16], Mutschke et al. 2001 [17]), and applying a suction/blowing forces on the flow (Arcas & Redekopp 2004 [18], Delaunay & Kaiktsis 2001 [19], Leu & Ho 2000 [20]). On the other hand, passive control methods do not require an external energy input, but rather depend on changing the shape and the geometry of the bluff body in such a way to suppress the vortex shedding and to decrease structural vibrations and noise. Some examples of these methods are changing the surface roughness of the body (Shih et al. 1993 [21]), using dimples (Bearman & Harvey 1993 [22], Choi et al. 2006a [23]), using a helical wire (Lee & Kim 1997 [24]), using a splitter plate (Anderson & Szewczyk 1997 [25], Hwang et al. 2003 [26], Kwon & Choi 1996 [27], Ozono 1999 [28]), and using transverse & longitudinal grooves (Lim & Lee 2002 [29]). The decision whether to choose one of these two methods depends on the application and the feasibility of changing the geometry or exerting an external force on the body.

The longitudinal grooves of the cactus are thought to control passively the flow suppressing the vortex shedding, which will lead in consequence to the drag reduction. Bushnell (1991) [30] suggested that the grooves play an important role in drag reduction. Moreover, Abboud et al. [31] found that the wake of the cactus has significantly lower fluctuations than the smooth circular cylinder.

C. Thesis Objective

The objective of this thesis is to study the flow behind a cactus shaped cylinder and compare it to the flow behind a circular cylinder. To achieve this objective, Particle Imaging Velocimetry (PIV) technique will be used to describe the flow qualitatively and quantitatively. Moreover, the effect of the cactus grooves on the flow will be also

investigated using the same technique; explaining their effectiveness in suppressing the vortex shedding at high Reynolds numbers.

CHAPTER II

EXPERIMENTAL METHODS

Experiments were carried out in a wind tunnel to investigate the flow fields around a cactus shaped cylinder with 8-longitudinal grooves that are parallel to the cylinder's axis. The flow fields around a circular cylinder were also studied to allow the comparison between the two models, which will elucidate the improved aerodynamic behavior of the cactus resulted by its grooves. Particle Imagining Velocimetry (PIV) technique was used to visualize the flow in the wake of both models in addition to the flow near the cactus grooves. PIV was chosen because it can give a complete flow description at each instant of time shedding the light on the mechanisms that governs the flow. The flows behind both models were tested at three wind nominal inlet speeds of 14, 30.5, and 47 m/s. The flow upstream velocities for both models were measured at the center line of the flow, 1.6D away from the model.

The models were tested at Reynolds numbers of 5×10^4,1.1×10^5 and 1.7×10^5 which resemble the harsh wind storms in the deserts.

A. Wind Tunnel

The experimental study on the two models was done in an open loop L-shaped wind tunnel manufactured by Engineering Laboratory Design (ELD). The wind tunnel consists of three major parts which are the convex bell shape nozzle, test section, and a big suction fan. The tunnel inlet and outlet were open to the lab space, and the loop length between the two ends was approximately 17 m. Care was taken to situate the

tunnel far enough from the lab walls to avoid possible interferences and disturbances to the inlet flow. The power rating of the suction fan is 25 hp, and operates at variable frequencies from 5 to 50 Hz allowing the wind speed in the test section to vary approximately from 3 to 50 m/s with increments of 1 m/s. The test section has dimensions of 18in x18in x36in, and it has a square cross sectional area that is perpendicular to the flow direction. Moreover, the test section's walls are made of Plexiglass sheets. The air flow in the test section is uniform with a turbulence intensity less than 5%. In addition, the ratio of the area of the inlet of the wind tunnel to the area of the test section cross section is approximately 14.7. The convex bell shaped nozzle has honeycombs to straighten the flow in the test section.

Figure 2: L-shaped wind tunnel

B. Test Models

Two models were used in the experimental study. Particle Image Velocimetry (PIV) technique was applied to visualize and study the flow wake of the two models. The first model is a smooth circular shaped cylinder of diameter of D=69 mm and with aspect ratio of 6.53. The other model is a cactus shaped cylinder of same diameter and aspect ratio as the circular cylinder. The cactus cylinder has 8 axes of symmetry, and 8

U-shaped transverse grooves that are 45 degrees apart. The height of a single groove is approximately L= 5.7mm, and its internal diameter is 54 mm resulting to depth to diameter ratio of 0.082 which is close to biologically prevailing value of 0.07 (Geller & Nobles 1984). The cactus dimensions and shape were chosen according to a real saguaro cactus plant. The shapes and the dimensions of a circular and cactus cylinders are shown in Figure 3 with their orientations.

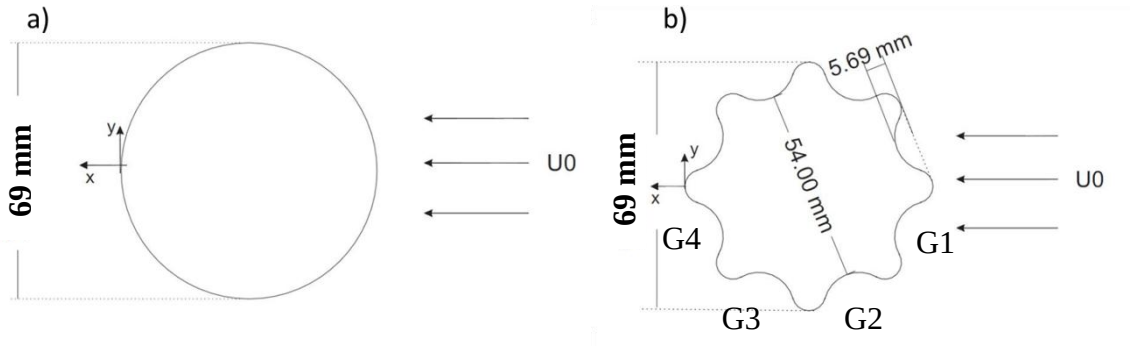

Figure 3: Experimental models' cross sections

Two configurations of the cactus will be tested. The first one is the cactus installed in such a way that the apex coincides with the upstream divider streamline as shown in Figure 3-b and it will be referred as “Cactus” throughout this thesis. The second one is the cactus being rotated 22.5 degrees around its central axis from the initial position of the first configuration as shown in Figure 4. This configuration will be referred as “Rotated Cactus” throughout this thesis.

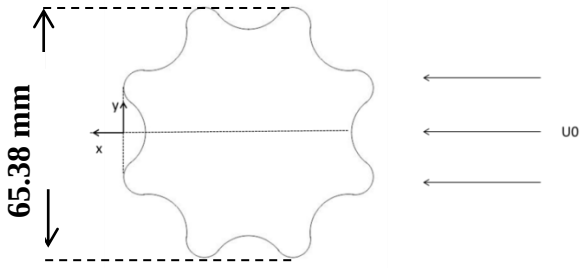

Figure 4: The rotated cactus model configuration

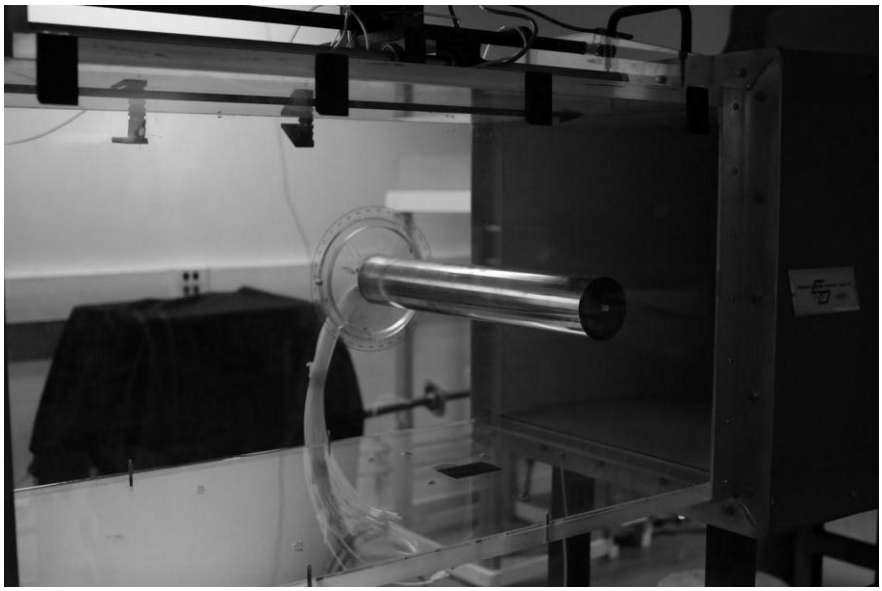

Figure 5: Picture of the test model installed in the test section

C. Particle Imaging Velocimetry or PIV Setup

The wake of the test models and the grooves of the cactus model were investigated using an in-house PIV system. The experimental setup is shown in Figure 6. It consists of dual head ND-YAG laser (Big Sky/Quantel, MN, USA) with a maximum energy per pulse of 180 mJ, and pulse duration of 6 ns. The 6 mm laser beam is formed into a 3 mm thick vertical laser sheet using a set of lenses and mirrors. The laser sheet is parallel to the flow and perpendicular the cylinder model central axis, and it is situated near the mid span of the model. For the immediate wake investigation, the laser sheet is placed to illuminate an area that extends from the model's trailing edge up

to two diameters downstream of the model. For the cactus grooves investigation, the laser sheet is moved upstream to illuminate each groove. The lower grooves labeled G1, G2, G3, and G4 as shown in Figure 3-b were investigated.

Olive oil 1 μm droplets generated by a six-jet atomizer (Model 6309, TSI, IL, USA) were seeded in order to visualize the flow. The seeder is placed outside the bell-shaped inlet of the wind tunnel to ensure uniform distribution of the seeds in the flow. These tracer particles were illuminated by a laser sheet, and images of the illuminated particles were recorded using a high speed cross-correlation CCD camera (Sensicam SVGA, PCO, Germany). The camera takes 12 bit image pairs at a rate of 4 Hz and with a resolution of 1280×1024 pixels. The camera is capable of a minimum inter-frame timing of 0.2 μs. For the immediate wake measurements, the field of view captured by the camera extends 2 diameters horizontally and 1.5 diameters vertically. For the groove measurements, a zoomed field of view was captured by the camera and extends 0.5 diameter horizontally and 0.3 diameters vertically. The dual laser and the camera trigger timings are provided by a 6 channel pulse delay generator (DG100, Thorlabs, NJ, USA) controlled by a custom LabView® program on a desktop PC. The inter-frame delay between the two laser pulses (dt) is set by the LabView® program to have pixel motion between 5 and 7 in order to decrease the number of particles that exhibit motion in the third dimension, and to improve the cross correlation between the two frames of the particle image pairs, improving the PIV correlation.

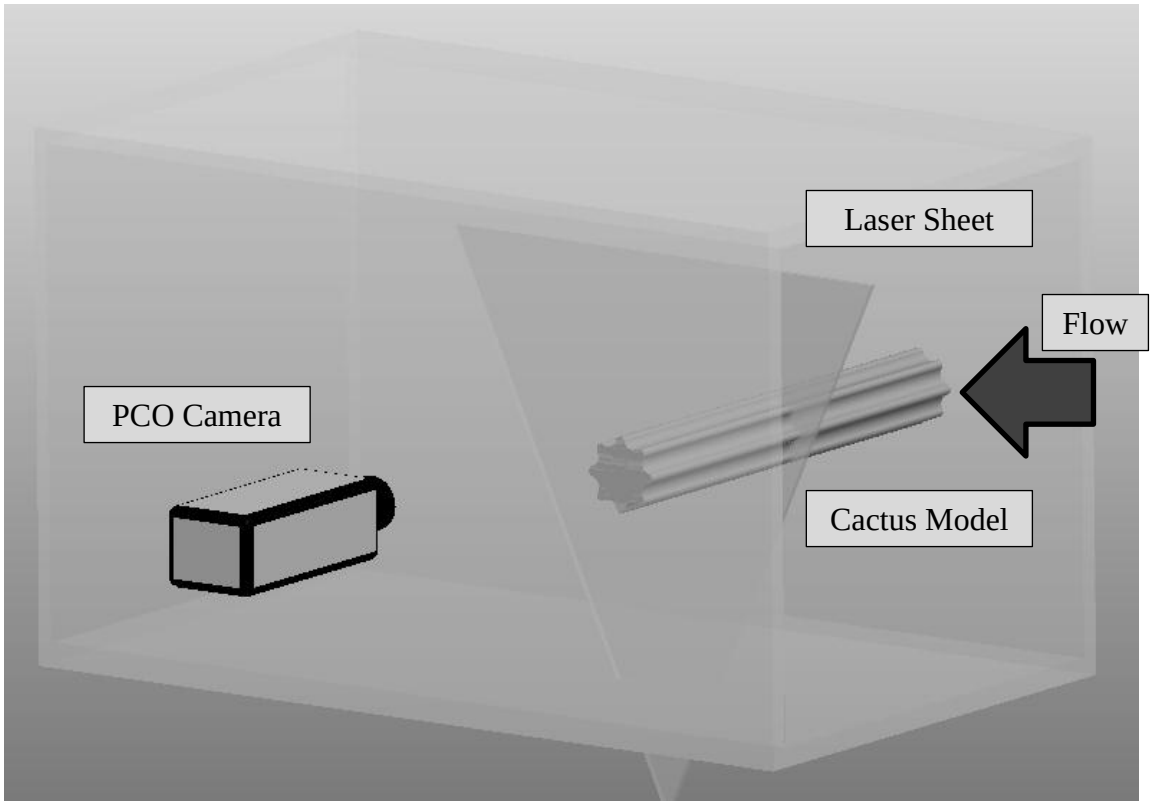

Figure 6: Sketch of the experimental setup of the test section

The raw images were processed using PIVLAB software (Han & Mungal, 2003) which is Matlab® based and it uses FFT cross correlation PIV processor. Each image pair is translated into a displacement vector field that is transformed upon dividing it by the inter-frame delay (dt) into a velocity vector field of the flow. Vector fields are post processed and filtered using a median and range filter and bad vectors were rejected. The percentage of bad vectors was not exceeding 3~4%. The vector spacing was approximately 1.8 mm and 0.3 mm for the wake flow and grooves flow, respectively. At least 650 vector fields were taken for each test in order to contribute to significant mean and turbulence statistics analysis.

Moreover, the laser sheet was moved to illuminate the upstream of the model. The laser illuminated an area that is extended from the prevailing model's edge into 2

diameters upstream. Particle images were taken and processed, and the upstream velocity (U_0) for each test was taken at the centerline of the flow that is 1.6 diameters far from the model in the upstream.

D. Wake and Grooves PIV Vector Fields Analysis

The instantaneous vector fields for each test were averaged using a Matlab® script into a single vector field that gives a mean description of the flow. The velocity magnitude was normalized by dividing it by the upstream velocity (U_0). Turbulence statistics were computed for each case in order to describe the flow fluctuations and give a sense of the temporal changes of the flow. The equation that is used to compute the turbulence intensity is:

$$u'^2 = \sum_{i=1}^{N}(u_i - \bar{u})^2/N \quad (1)$$

Where:

u'^2 : Stream wise turbulence intensity

u_i : Instantaneous stream wise velocity

$\bar{u}$: Averaged stream wise velocity

N : Total number of vector fields

Moreover, vortex fields were computed from the velocity vector fields using \least square differentiation method described in Raffel et al. (1998) [32]. The vector fields were further filtered by exponential filter. Average vortex fields were obtained for each case and it showed a positive vortex and a negative vortex. The instantaneous vortex fields were spatially averaged and were plotted on histograms for the immediate wake cases. The histograms showed two distinct peaks corresponding to the shedding of the vortices. Noting the periodic behavior of the flow, the vector fields were grouped

into 10 groups according to their spatial vorticity average giving a temporal sense of how the flow develops and changes with respect of time. This is achieved by taking a huge number of PIV image pairs, and it is useful since cinematic PIV is impossible to be done using the current equipment.

CHAPTER III

RESULTS & DISCUSION

The PIV results of the immediate wake for both test models are presented and discussed in this chapter. Moreover, the PIV results of the cactus grooves will be also discussed explaining the shedding in the immediate wake of the cactus. Comparisons between the cactus immediate wake and the smooth circular cylinder will be deliberated throughout this chapter using velocity vector fields and contours in addition to turbulence statistics and vortices analysis. The chapter will be divided into two big sections; one for the immediate wake analysis and the other will be for the grooves analysis.

A. Immediate Wake Flow Analysis

PIV experiments were done to investigate the flow in the immediate wake of the test models. In the following analysis, the coordinate axes (x & y) are normalized by the diameter of the projection of the model on a vertical plane parallel to the models centerline (D=69 mm for Cactus and Circular cylinder and D=65.38 mm for the Rotated Cactus). Moreover, the velocities are normalized by the upstream velocities U0 listed in the Table 1 for each case.

Table 1: The parameters of the test experiments

Blower Frequency (Hz)	15		30		45	
Nominal Re	50,000		110,000		170,000	
Actual Re	49,680	47,840	109,480	107,640	170,200	170,200
Actual Velocity (m/s)	10.8	10.4	23.8	23.4	37	37
Model Cross Section	Cactus	Circle	Cactus	Circle	Cactus	Circle

1. Mean Flow Analysis

The average vector fields for the two configurations of the cactus and the smooth circular cylinder for the three tested Reynolds numbers are shown in Figures 7, 8 and 9. These average vector fields are got from averaging at least 650 instantaneous vector fields describing the mean flow that is exhibited for each case. It is noticed from the vector fields that there are two big vortices of opposite spinning direction which are residing in the immediate wake of both models for all the tested speeds. Upon examining the fields carefully, the wake of the Cactus has smaller vortices than the circular cylinder vortices for the higher tested Reynolds numbers, but has the same size of vortices with the circular cylinder at the lowest tested Reynolds number of 50,000; however, the Rotated Cactus vector fields reveal the largest vortices for all the tested Reynolds number. Furthermore, it is shown in all the average vector fields that the flow starts to straighten. Therefore, the flow in all the tested cases starts to recover after at least x/D = 1.

Contours plots of normalized average stream wise velocity component (u/U_0) and the normalized vertical velocity component (v/U_0) are shown in Figures 10,11,12,13,14 and 15 in order to expand the analysis of the immediate wakes of the test

models. The white dashed lines represent the linear profiles that are plotted in Figure 16. Inspecting the stream wise velocity contours (u/U_0), the Cactus has smaller wake than the circular cylinder for the two higher tested Reynolds number, and it has approximately the same wake of the circular cylinder for the lowest tested Reynolds number. Moreover, the cactus wake is spatially closer to the cylinder's surface. This depicts faster flow recovery and less flow disturbance for the cactus. The flow is symmetric as it is manifested in the contours, especially the (v/U_0) contours and the linear profile plots.

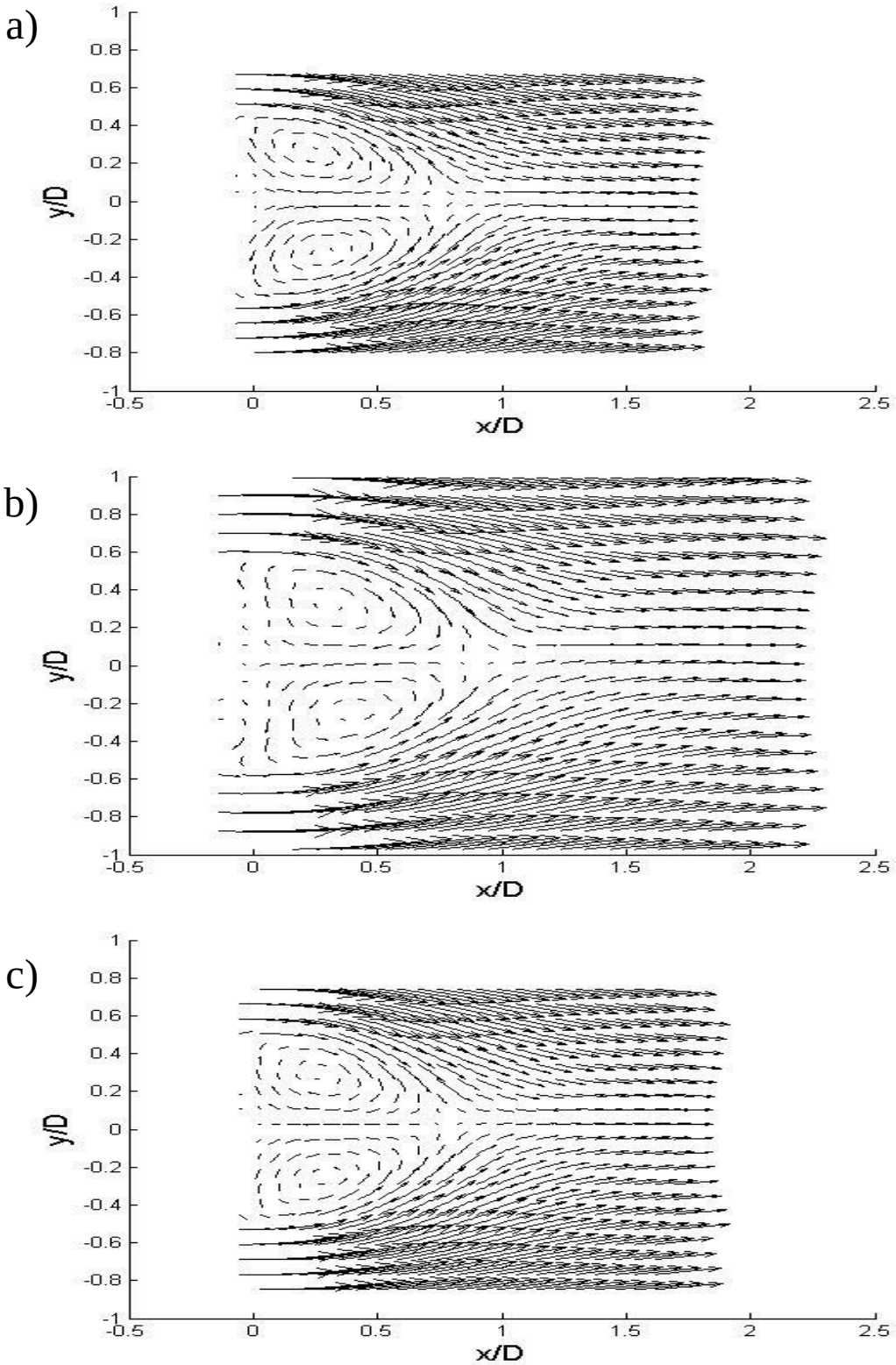

Figure 7: Average Vector fields at Re=50,000 for a) Cactus, b) Rotated Cactus, and c) Circular cylinder

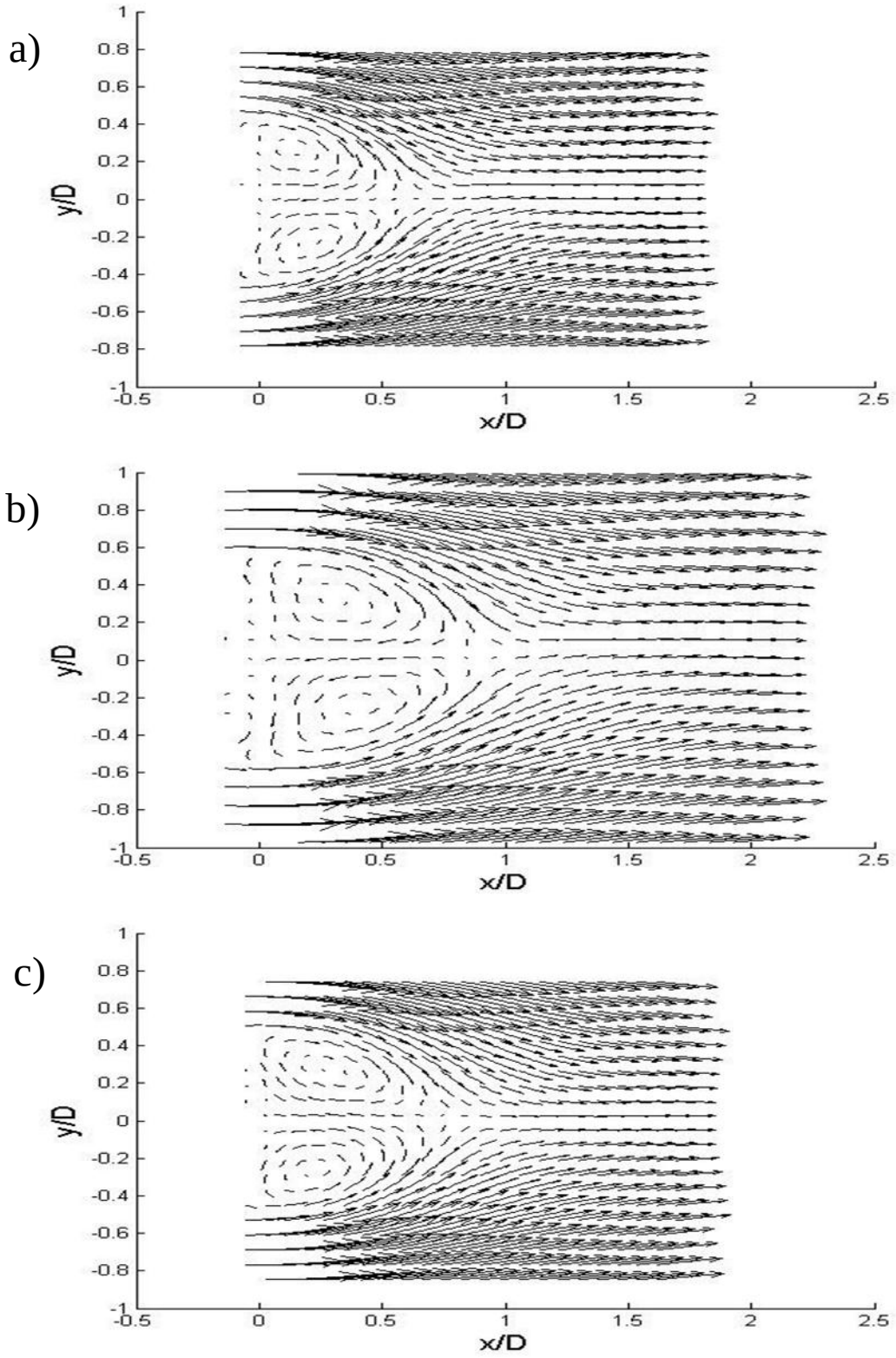

Figure 8: Average Vector fields at Re=110,000 for a) Cactus, b) Rotated Cactus, and c) Circular cylinder

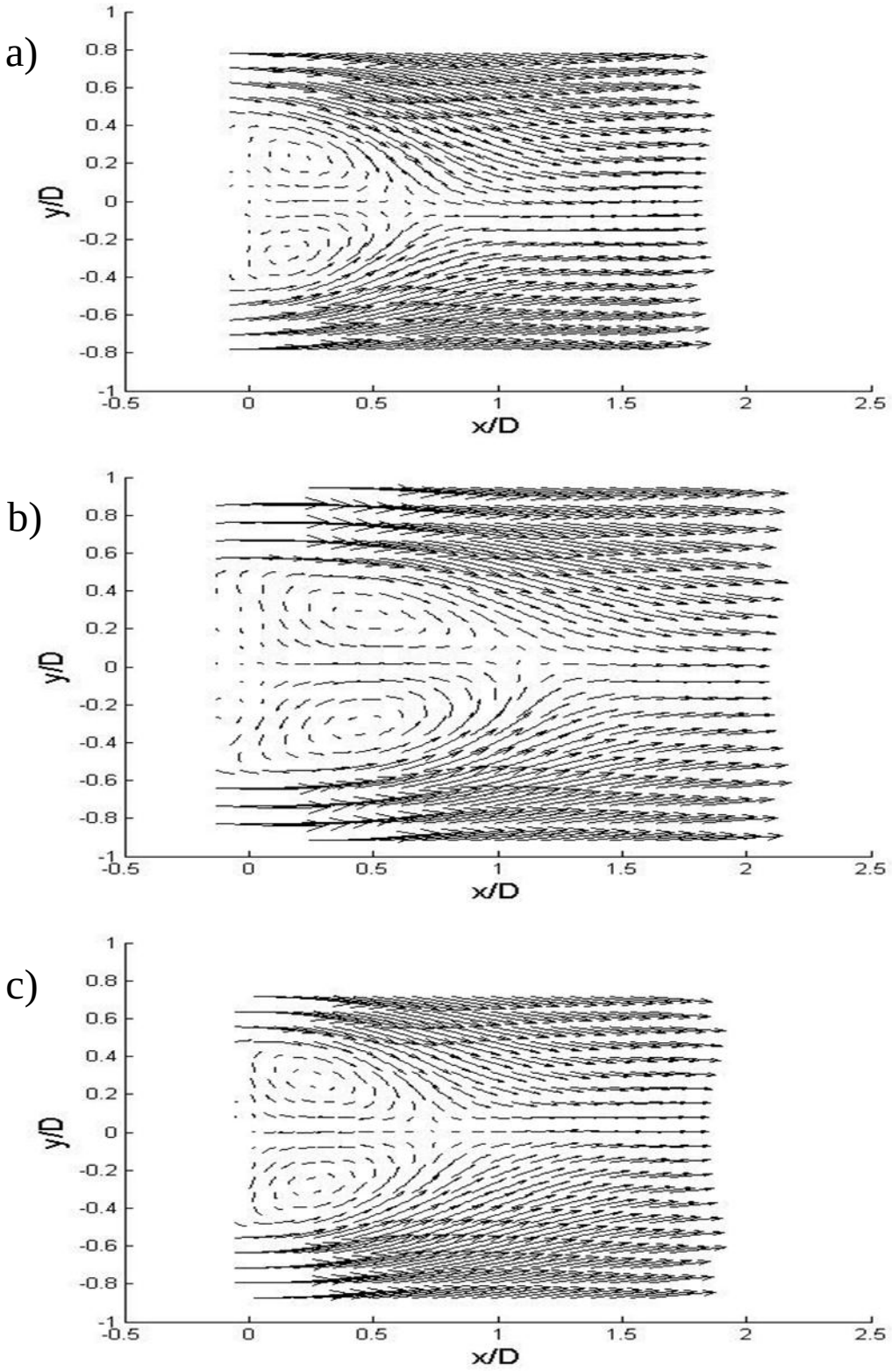

Figure 9: Average Vector fields at Re=170,000 for a) Cactus, b) Rotated Cactus, and c) Circular cylinder

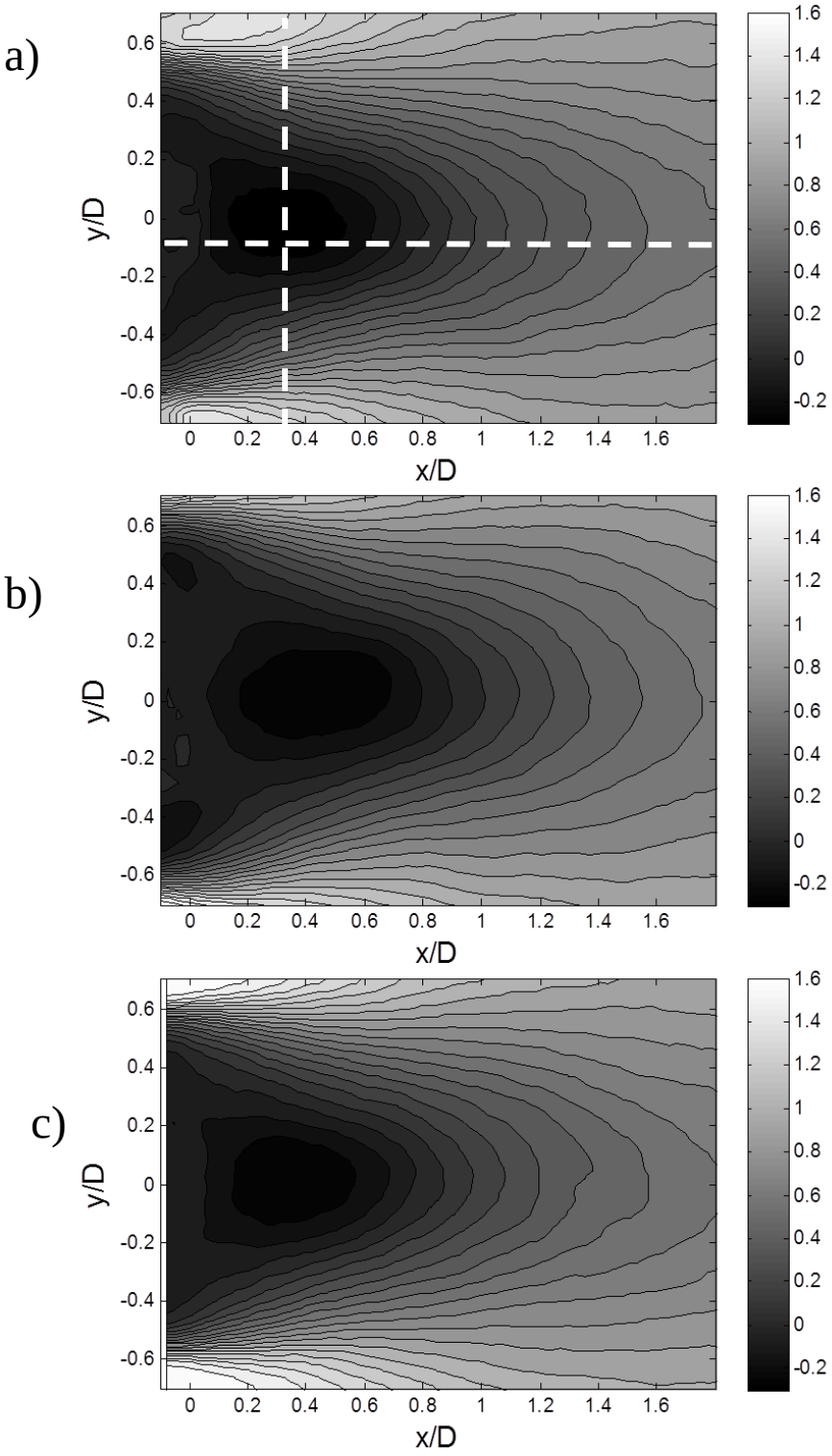

Figure 10: Stream wise velocity u/U0 contours at Re=50,000 for a) Cactus, b) Rotated Cactus, and c) Circular cylinder

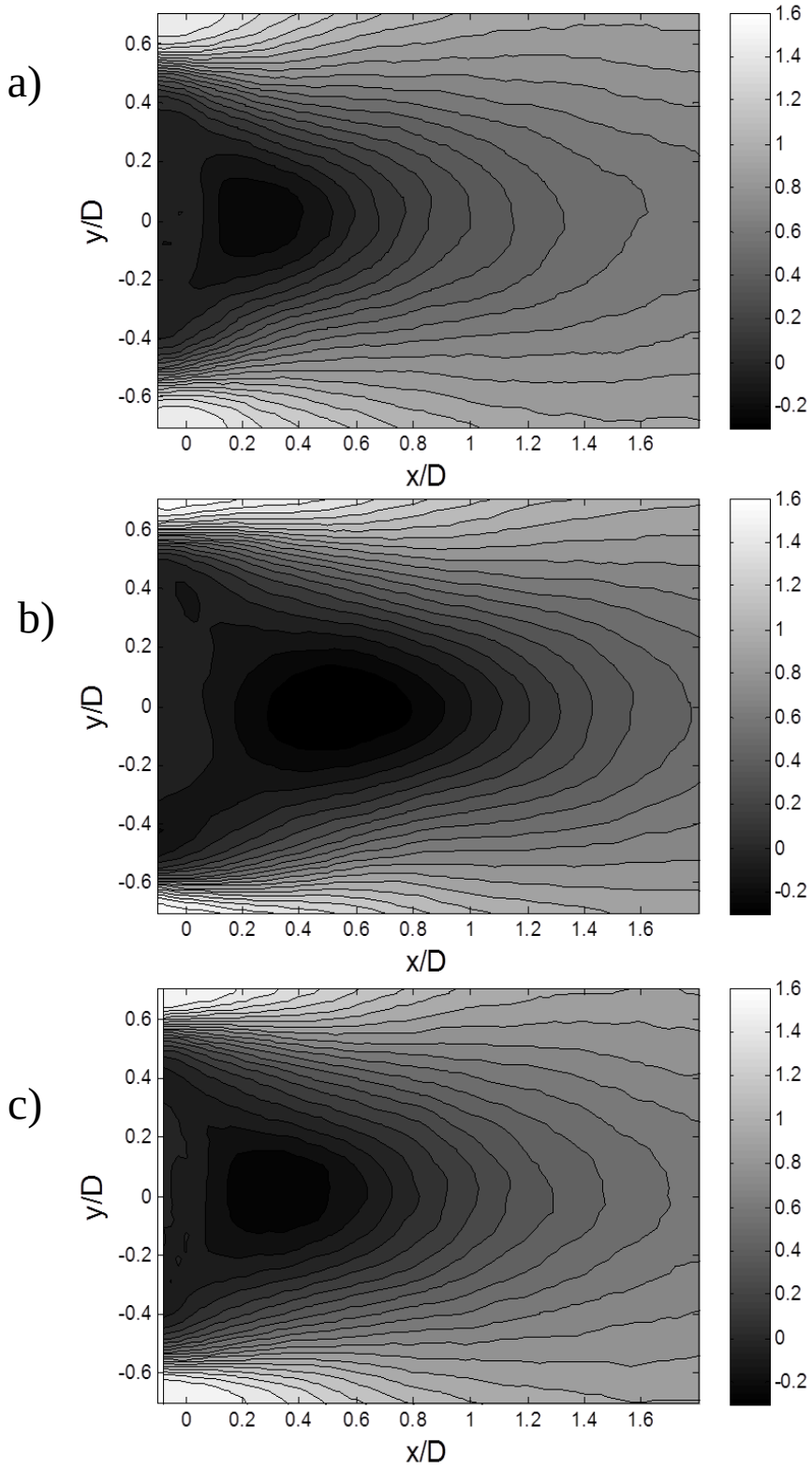

Figure 11: Stream wise velocity contours u/U0 at Re=110,000 for a) Cactus, b) Rotated Cactus, and c) Circular cylinder

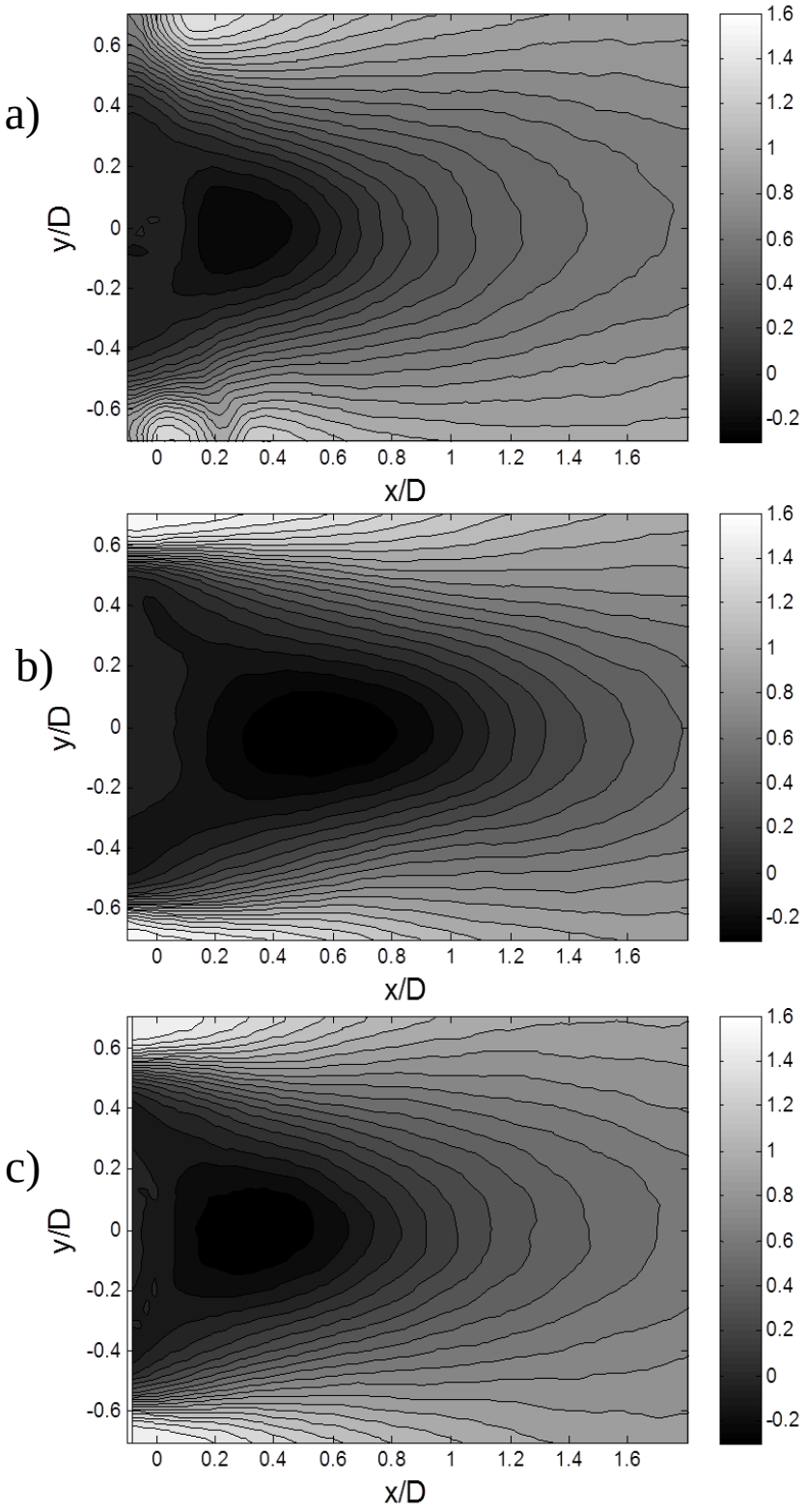

Figure 12: Stream wise velocity contours u/U0 at Re=170,000 for a) Cactus, b) Rotated Cactus, and c) Circular cylinder

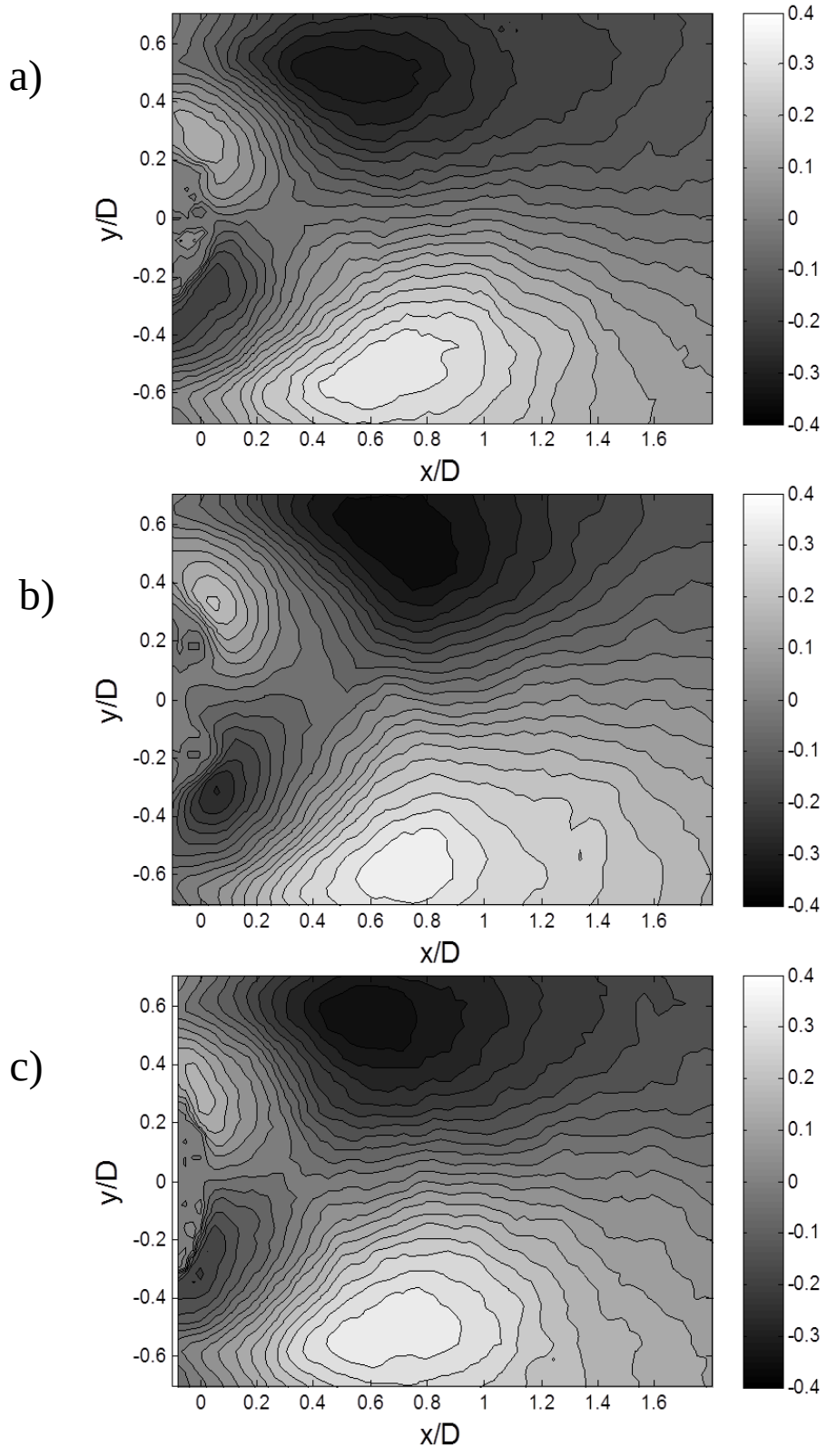

Figure 13: Vertical velocity v/U0 contours at Re=50,000 for a) Cactus, b) Rotated Cactus, and c) Circular cylinder

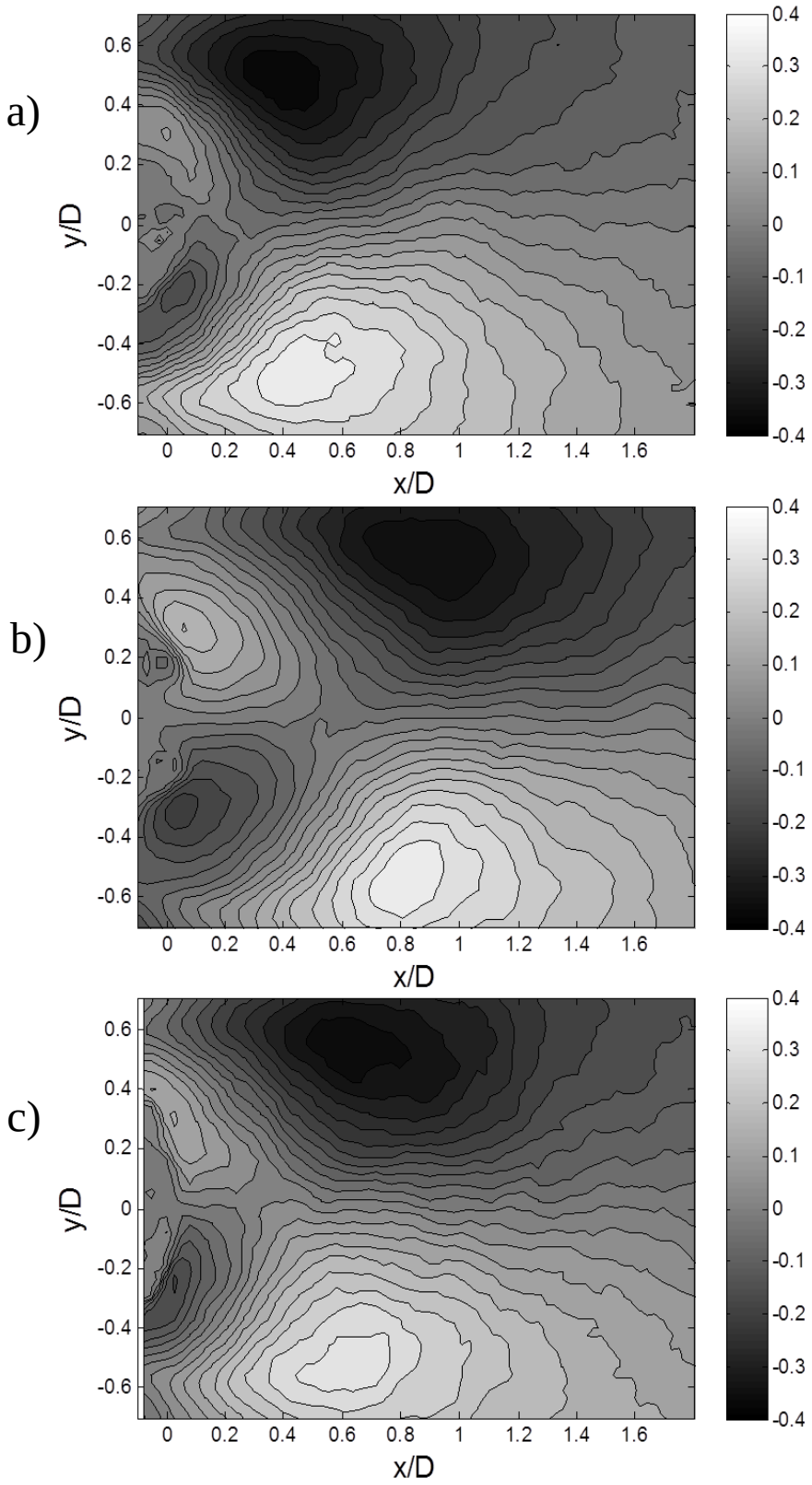

Figure 14: Vertical velocity v/U0 contours at Re=110,000 for a) Cactus, b) Rotated Cactus, and c) Circular cylinder

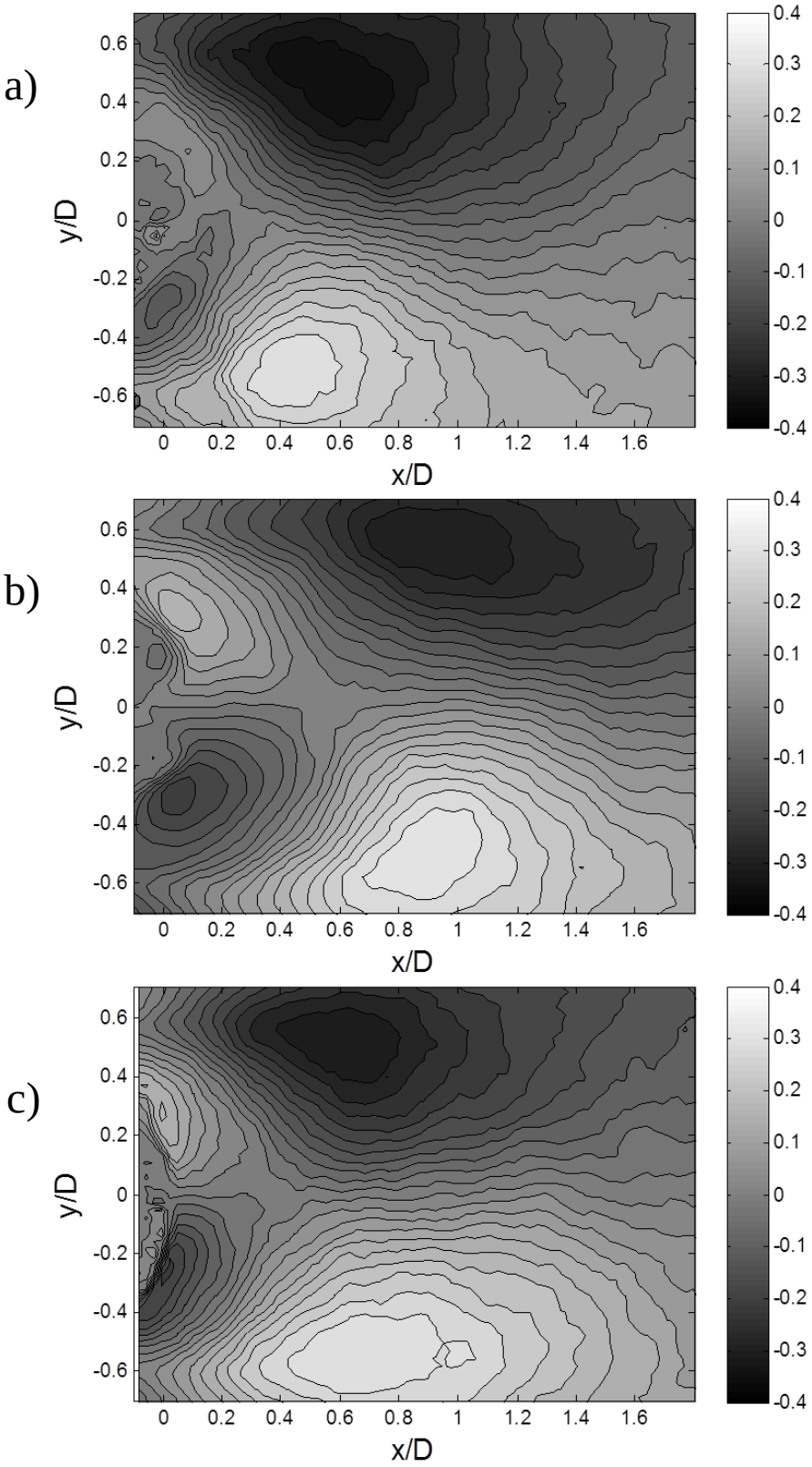

Figure 15: Vertical velocity v/U0 contours at Re=170,000 for a) Cactus, b) Rotated Cactus, and c) Circular cylinder

However, the rotated cactus exhibits larger wakes than the cactus and the circular cylinder for all tested Reynolds numbers as shown in Figure 16. Its wake is elongated downstream, and it is spatially relatively far from the model's surface. This behavior is also manifested in the vertical velocity (v/U_0) contours.

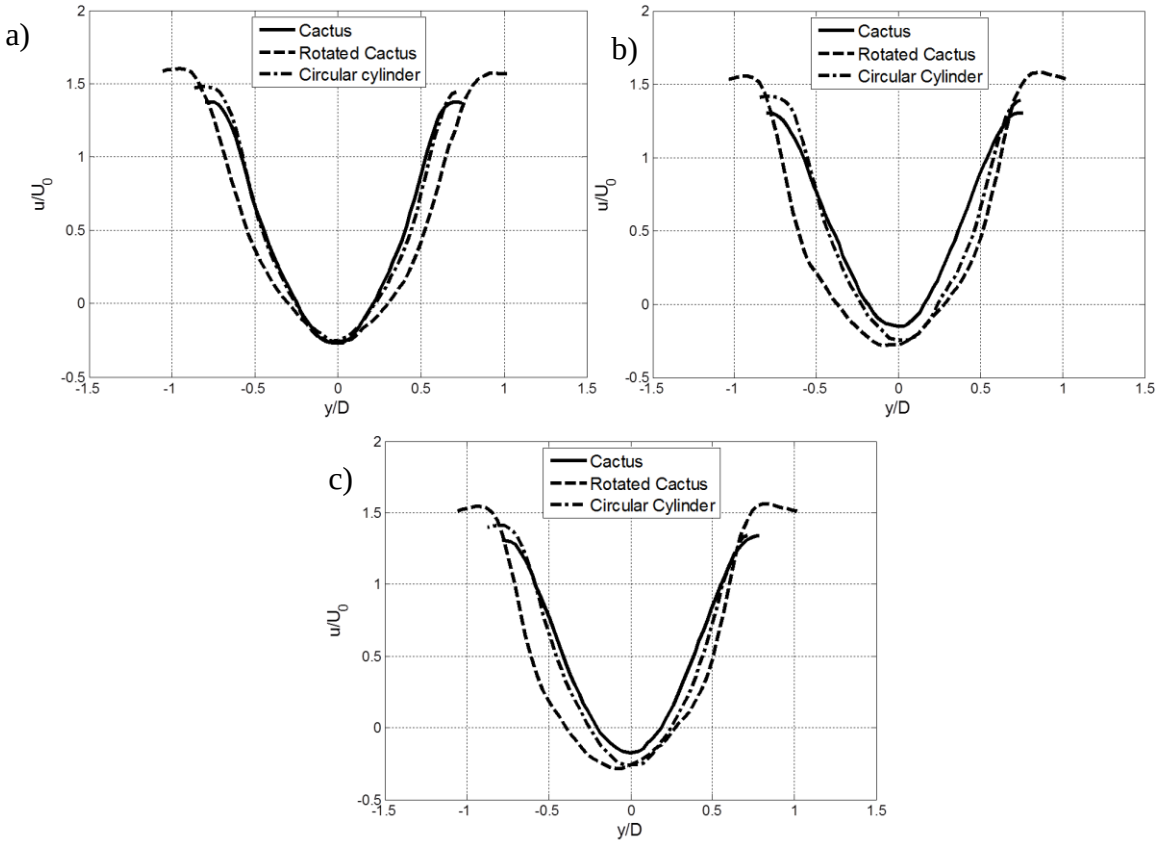

Figure 16: Linear profiles plots for u/U_0 at x/D = 0.4 a) Re=50,000 b) Re=110,000 c) Re=170,000

Linear profiles of the stream wise velocity (u/U_0) at x/D = 0.4 for all the cases were plotted in Figure 16. From these plots, it can be concluded that backflow is weaker in the cactus case than the circular cylinder case. Moreover, it is noticed that the rotated cactus backflow is the strongest. Furthermore, the cactus wake is the smallest given that its profile curve is the narrowest, then the circle cylinder wake, then the rotated cactus.

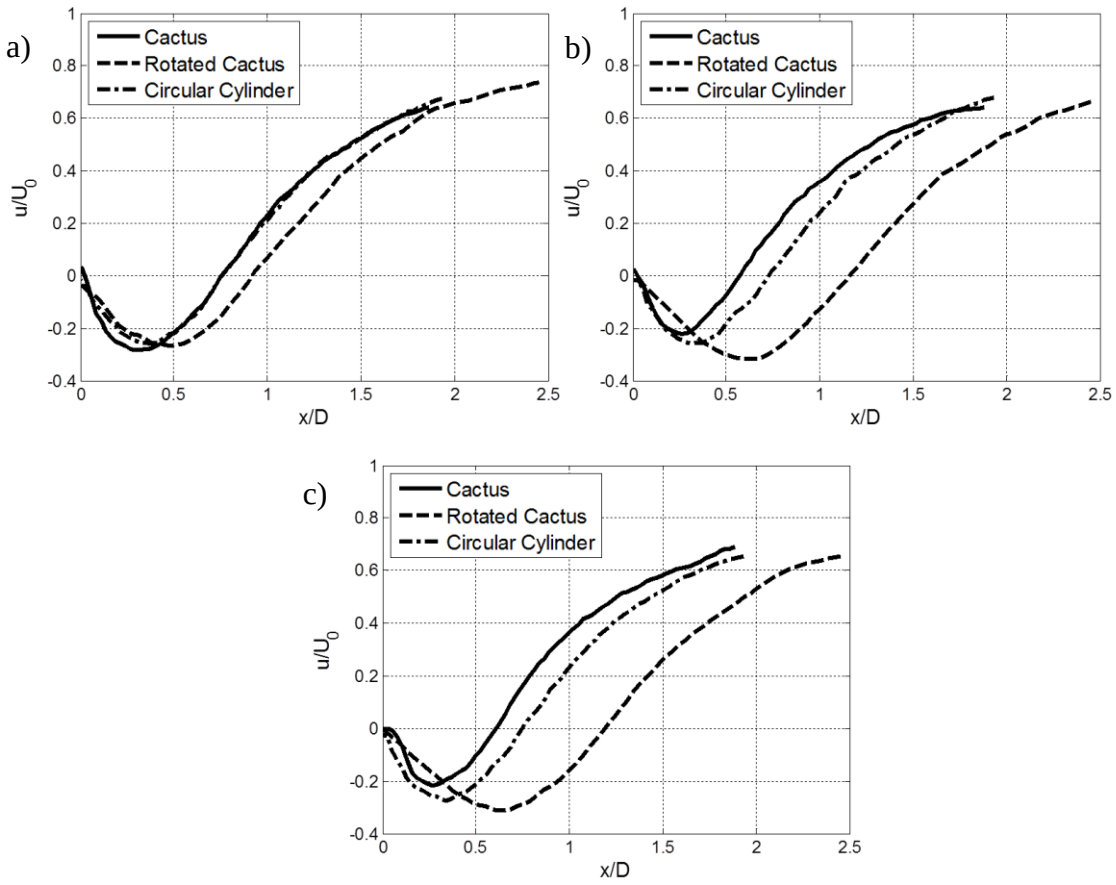

Figure 17: Linear profiles plots for u/U_0 at y/D = 0 a) Re=50,000 b) Re=110,000 c) Re=170,000

The linear horizontal profile plots of the stream wise velocity (u/U_0) at y/D=0 for all tested Reynolds numbers are shown in Figure 17. There is no significant difference between the cactus and the circular cylinder at the lowest tested Reynolds number of 50,000. However, for the two higher tested Reynolds numbers (110,000 & 170,000), the cactus showed smaller wake as it possess narrower 'U' shaped plots, and it possess weaker backflows as manifested in Figure 17-b-c. Moreover, the flow heals faster in the cactus case than the circular cylinder. The rotated cactus exhibits wider 'U' shaped plots and have the strongest backflow; in addition, it exhibits the slowest flow healing as depicted in the Figure 17 for all tested Reynolds numbers.

2. Turbulence Statistics Analysis

Turbulence statistics were computed from at least 650 instantaneous vector fields for each tested speed in order to analyze the turbulence and the shedding in the immediate wake of both the cactus cylinder and the circular cylinder. Turbulence intensities give a sense of how the flow is varying around its average. The normalized stream wise turbulent velocity ($\sqrt{u'^2}/U_0$) contours for all tested speeds are shown in the Figures 18, 19 & 20. Studying the contours, it is noticed that both configuration of the cactus have lower turbulent stream wise velocity than the circular cylinder for all tested speeds. This portrays that the cactus wake experiences significantly lower fluctuations in the instantaneous stream wise velocity in its near immediate wake. Therefore, it can be concluded that the flow is steadier in cactus wake, meaning that the upper shear layer and the lower shear layer separates smoothly and interacts with each other in an organized mode. Moreover, it is shown from the contours that the Rotated cactus experiences turbulent region to be far from its surface and more turbulence intensities in the upper and lower shear layers. Furthermore, a more expanded analysis of the stream wise turbulent velocity is pursued in the linear profile plots at x/D=0.4 shown in Figure 21.

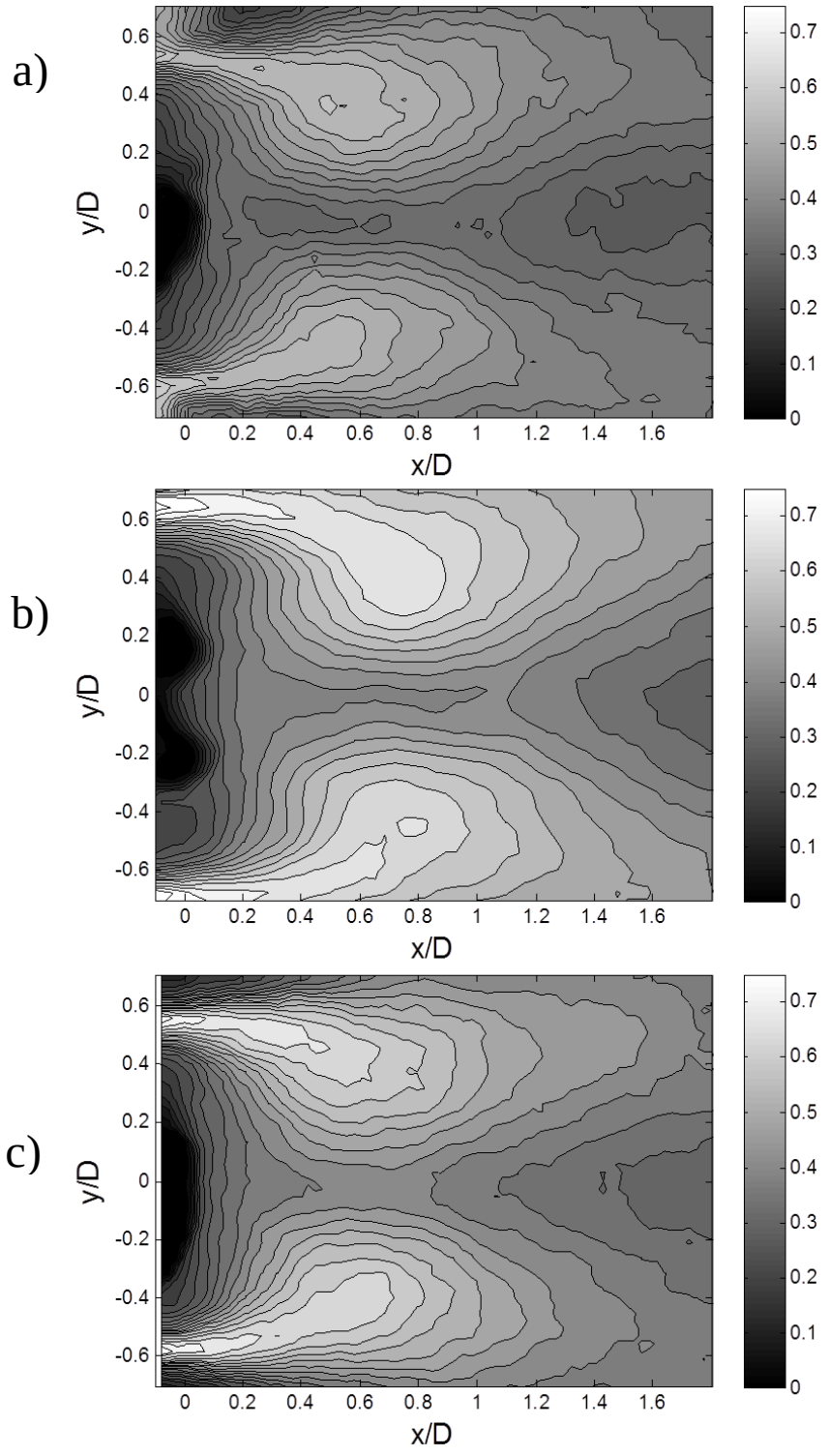

Figure 18: Horizontal turbulent intensity $\sqrt{u'^2}/U_0$ contours at Re=50,000 for a) Cactus, b) Rotated Cactus, and c) Circular cylinder

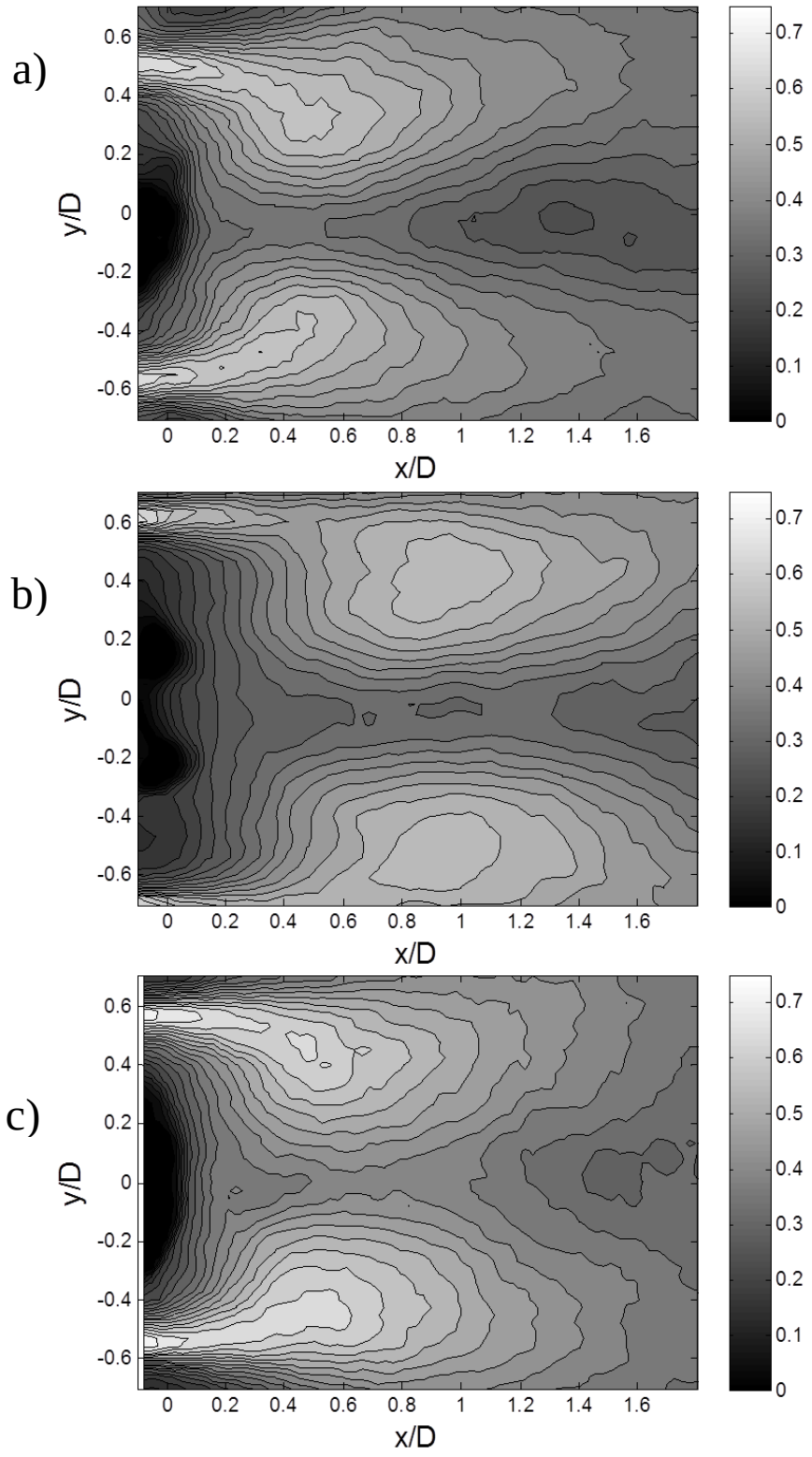

Figure 19: Horizontal turbulent intensity $\sqrt{u'^2}/U_0$ contours at Re=110,000 for a) Cactus, b) Rotated Cactus, and c) Circular cylinder

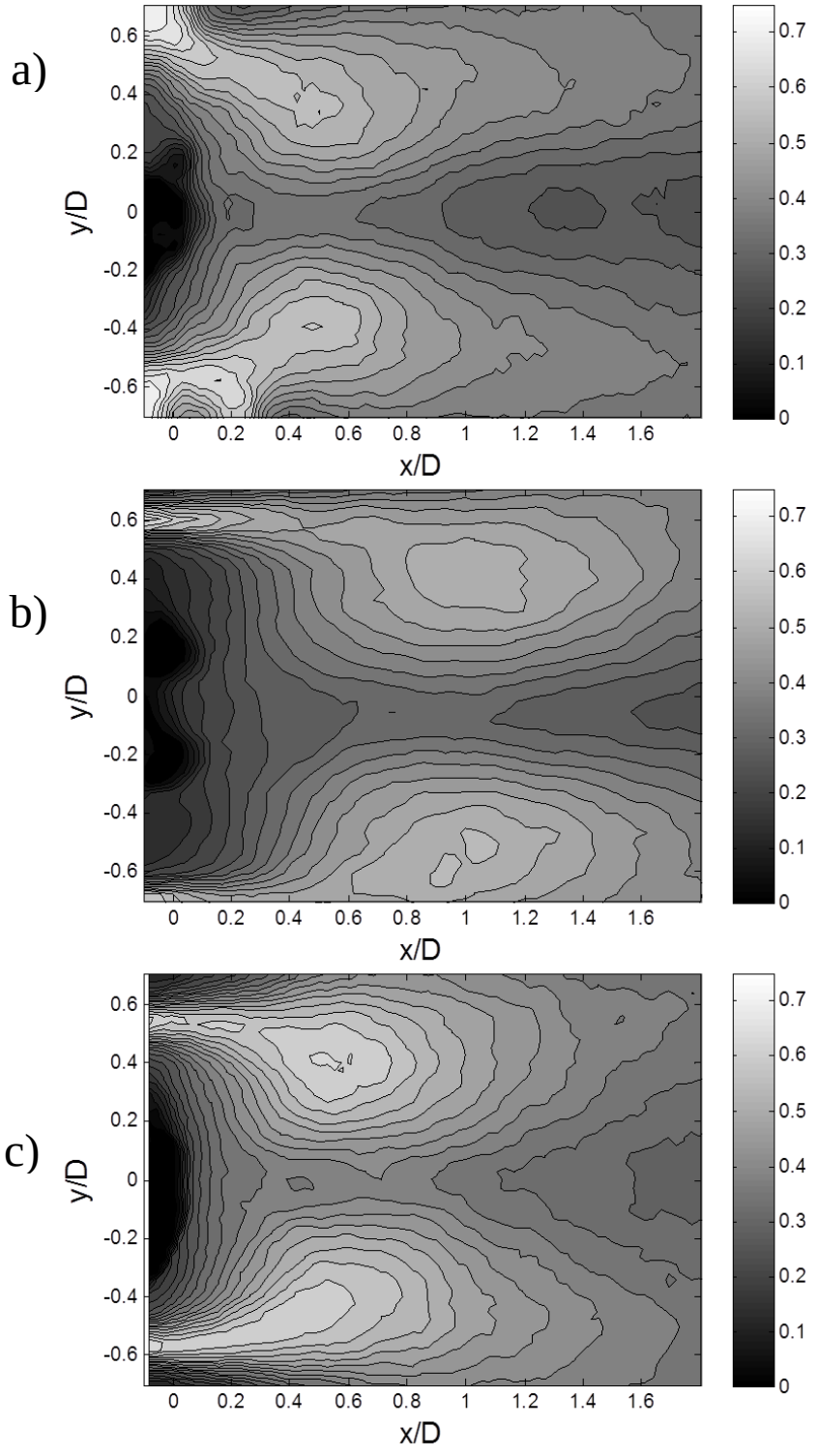

Figure 20: Horizontal turbulent intensity $\sqrt{u'^2}/U_0$ contours at Re=170,000 for a) Cactus, b) Rotated Cactus, and c) Circular cylinder

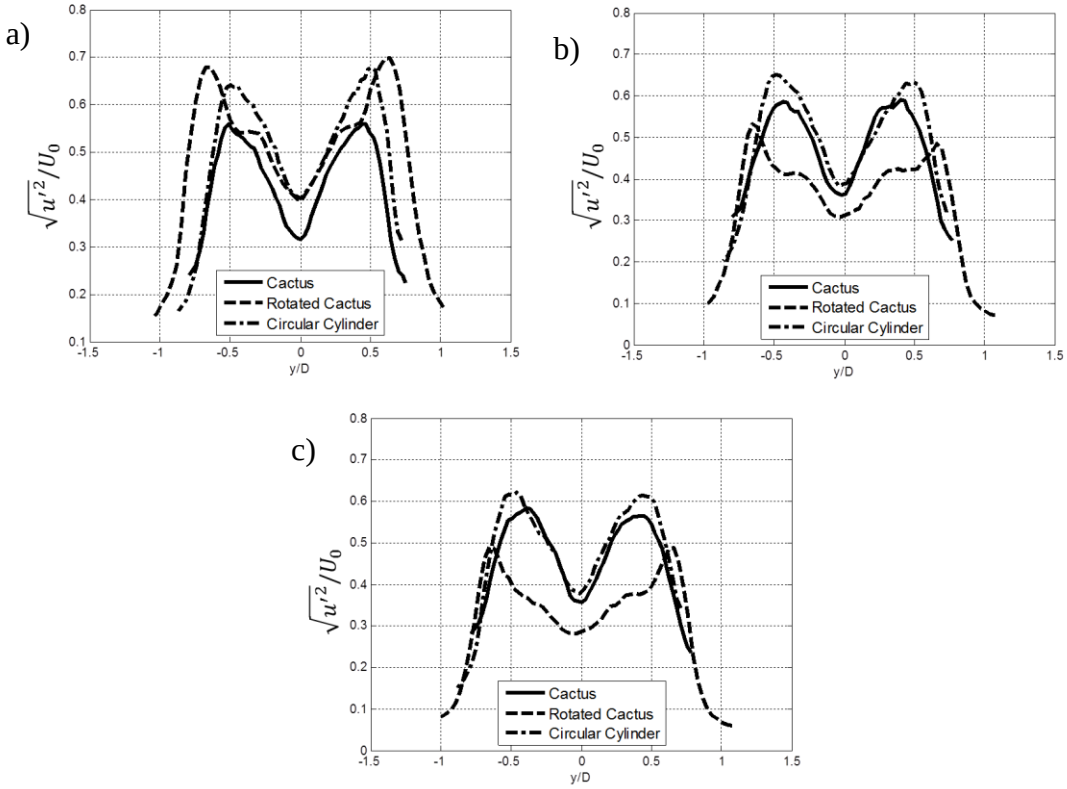

Figure 21: Linear profile plots of $\sqrt{u'^2}/U_0$ at x/D = 0.4 a) Re=50,000 b) Re=110,000 c) Re=170,000

Inspecting the stream wise turbulent intensity plots shown in Figure 21, it can be noticed that the cactus exhibits lower fluctuations than the circular cylinder for all tested speeds. Moreover, the rotated cactus exhibits significantly lower fluctuations than the cactus and the circular cylinders for the two highest tested Reynolds numbers. This means that the rotated cactus has much steadier immediate wake than the circular cylinder; concluding that the cactus cylinder behaves aerodynamically better than its counterpart circular cylinder.

3. Average Vortex Analysis

Average vortex fields are shown for the tested models at the three tested speeds in Figures 22, 23 & 24. These vortex fields add to the description of the immediate wakes of the cactus, as they show the distribution of the temporal averaged vortex structure for all the cases helping to understand furthermore the shedding.

The vortices intensities are normalized by (U_0/D) in order to allow comparison among the test cases. It is noticed that the cactus average vortex structure is spatially closer to the cactus surface and engulfing it. This suggests that the vortex shedding is uniform, i.e. the upper and lower shear layers separates in a clean periodic way reducing the level of turbulence and flow fluctuations. On the other hand, the upper and lower shear layers of the circular cylinder are spatially elongated towards the downstream, suggesting that these layers are interacting violently in the immediate wake.

The rotated cactus exhibits an intermediary form of the average vortex structure between the cactus and the circular cylinder. Its upper and shear layer are elongated towards the downstream, but they start to bend towards the cactus at x/D~ 0.6 as shown in Figures 22-b, 23-b, 24-b. Taking into consideration the stream wise turbulent velocity ($\sqrt{u'^2}/U_0$) contours plots, the vortex streets starts to develop away from the cactus surface resulting in significantly lower flow fluctuations. Therefore, the rotated cactus immediate wake exhibits the effects of delaying the separation of the boundary layer creating steadier wake.

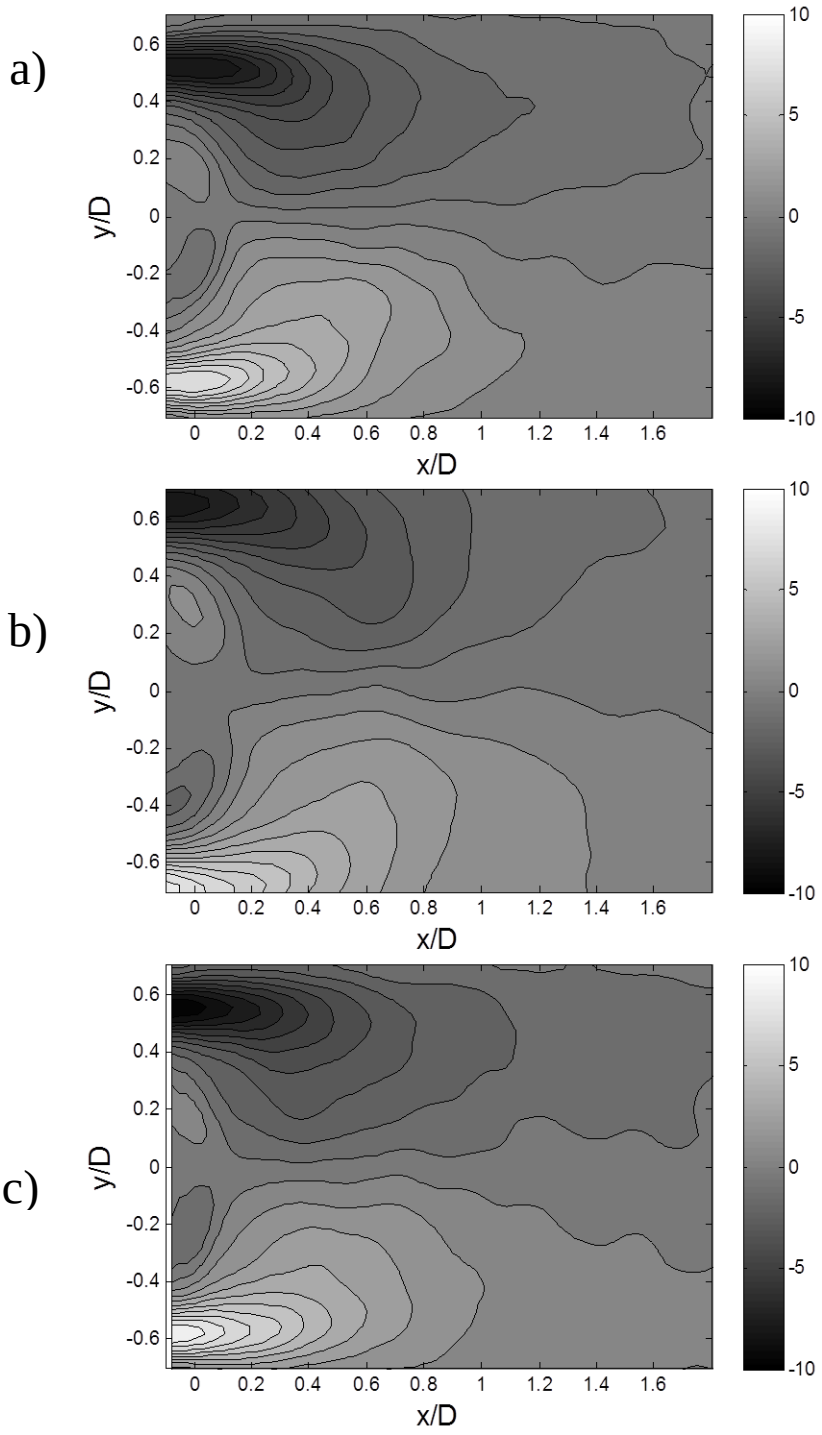

Figure 22: Normalized vorticity $\omega/(U_0/D)$ contours at Re=50,000 for a) Cactus, b) Rotated Cactus, and c) Circular cylinder

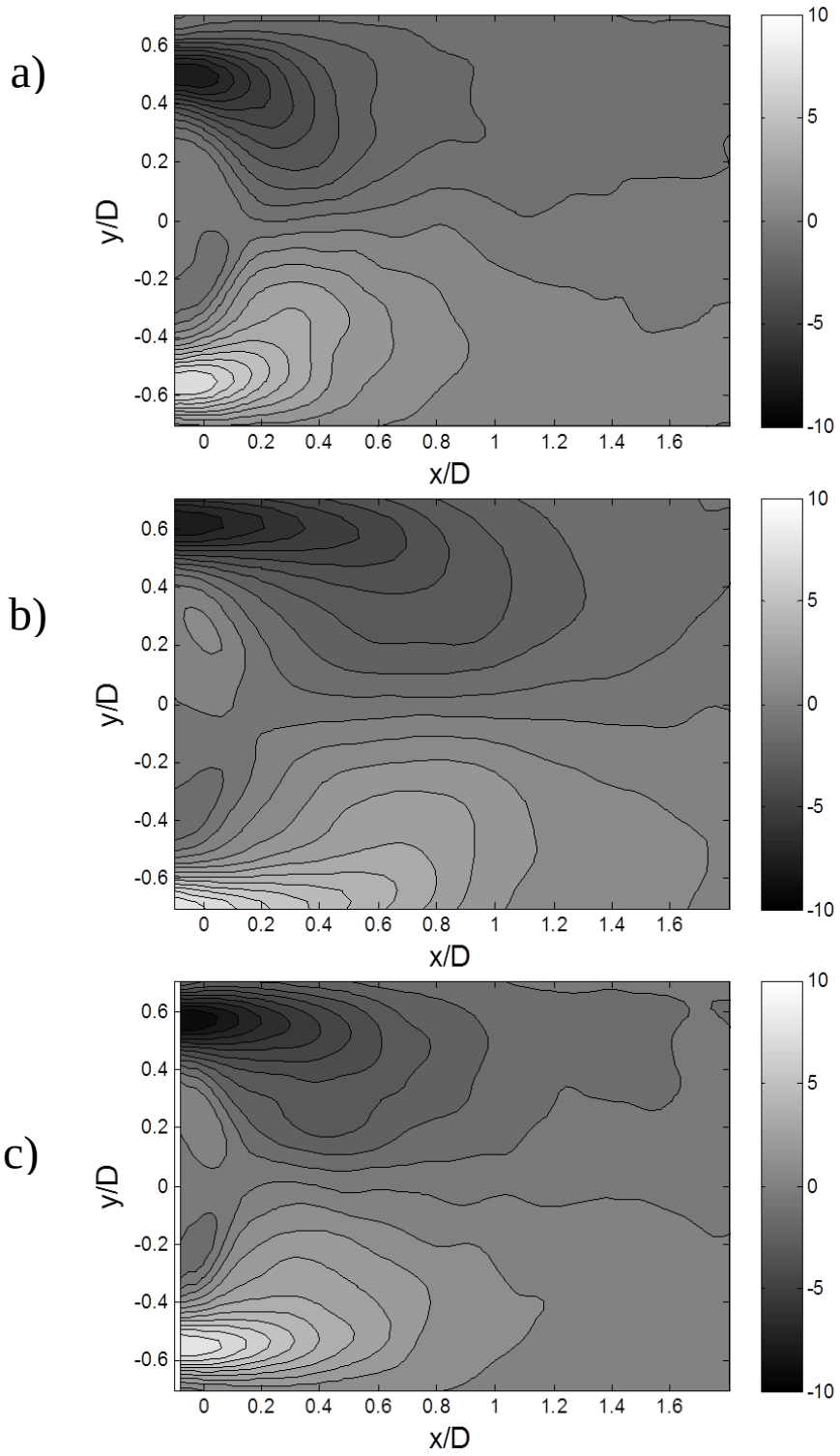

Figure 23: Normalized vorticity $\omega/(U_0/D)$ contours at Re=110,000 for a) Cactus, b) Rotated Cactus, and c) Circular cylinder

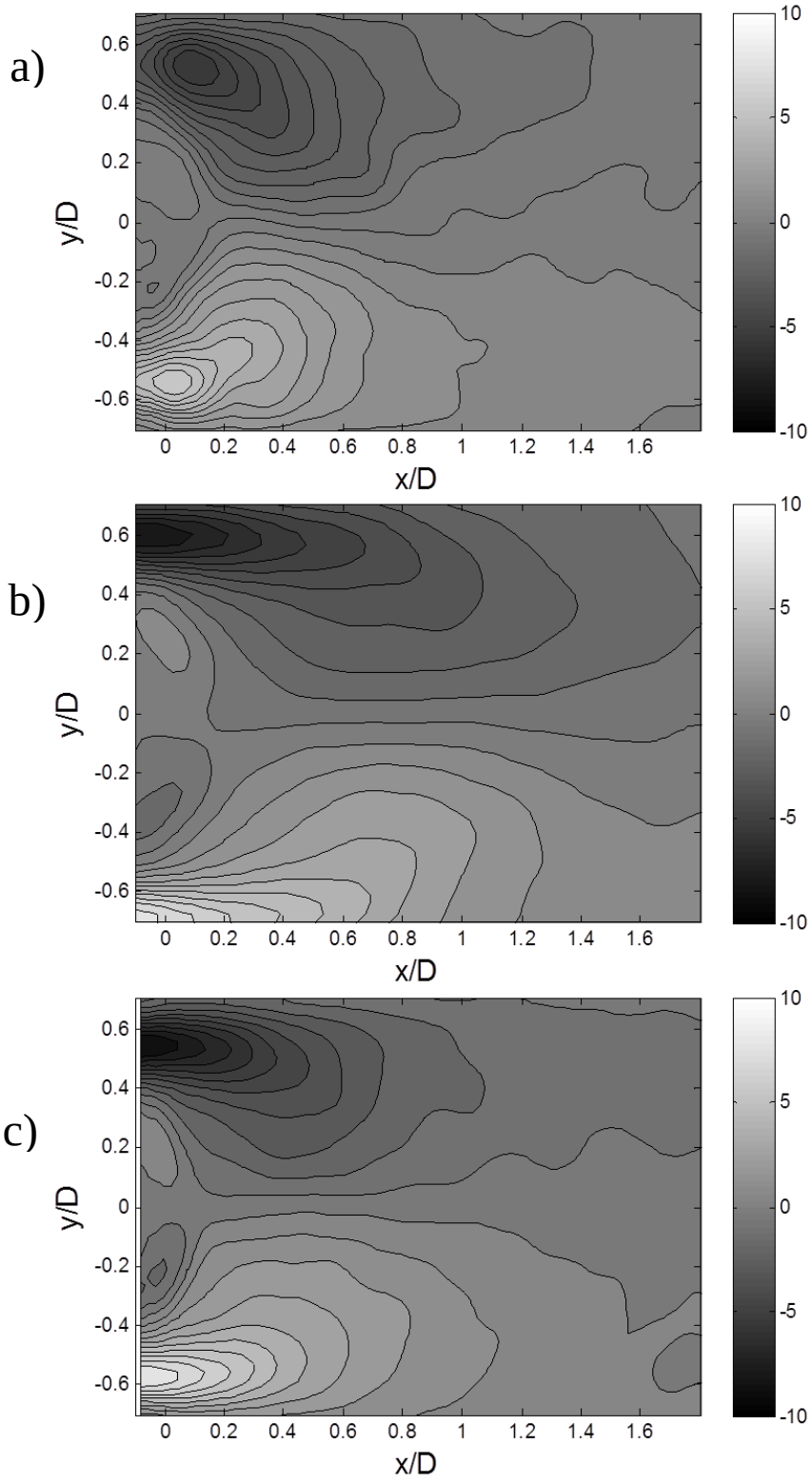

Figure 24: Normalized vorticity $\omega/(U_0/D)$ contours at Re=170,000 for a) Cactus, b) Rotated Cactus, and c) Circular cylinder

4. Instantaneous Flow Field Analysis

To gain insight into the vortex shedding process in the cactus and circular models, a simple conditional averaging process was implemented in which the spatially averaged wake vorticity magnitude was computed for each instantaneous flow field. Based on the instantaneous, spatially averaged wake vorticity, histograms were obtained as shown in Figures 25, 26 & 27.

They display two distinct peaks or groups of vorticity associated with the shedding of the oppositely signed shear layers off the top and bottom surfaces of the cylinder. At the lowest Re there is no significant difference in the shapes of the histograms for the cactus and circular geometries, while at the other two higher Re's the cactus model displays cleaner, more distinct peaks near $\omega D/u \sim +/- 0.5$ in comparison with more spread out histograms and less distinct peaks for the circular model. i.e. the region in between the peaks near $\omega D/u \sim 0$ the cactus has a lower number of vector fields in comparison with the circular cylinder. This indicates that the cactus boasts of cleaner and sharper vortex shedding, in which there are less violent interactions and collisions between the two shear layers as they peel in a more orderly fashion off the top and bottom cylinder surfaces. One can view the histogram as having two peaks, or it can be viewed as a continuous distribution of events since the shedding process is also continuous in time. So it is possible to divide the histogram into 10 sub-groups equally spaced along the vorticity axis, and to compute the time average flow field for each of the ten sub-groups. For each of the ten subgroups, the average velocity field superposed over the vorticity contours is shown in Figure 28 for the cactus model at Re = 170,000. The figure elucidates some of the instantaneous wake shedding dynamics through this simple decomposition method. When the shear layer from the

upper surface (CW vorticity) is at its maximum extent into the wake it experiences a necking process driven by the lower surface shear layer (CCW vorticity) which results in the detachment and roll up of a portion of the CW vorticity from the upper shear layer into the Karman street (**a-d**). The velocity field is characterized by a downwash that gets weaker as the dynamics progress in time. The upper shear layer recedes making way for the lower shear layer to occupy the wake space. At one point the extents of the upper and lower shear layers into the wake are nearly equal and the velocity field is characterized by upper/lower symmetry with no downwash/upwash (5-6). The process is then reversed where the lower shear layer experience a necking process as described earlier, with the vector field showing an upwash velocity (7-10). Similar dynamics were found for the circular model, except that the shed vorticity in the circular geometry where farther away from the model, while the vortices stayed closer to the cylinder surface in the cactus case. This crude flow decomposition was only possible because of its periodicity. This periodicity (~ 90 Hz at the higher Re) could not be captured with the slow PIV vector field acquisition (4 Hz); yet it was possible to reconstruct its salient time features *a posteriori* using the crude method described here. It may be possible to obtain further temporal information from these histograms under certain assumptions, but this effort has not been attempted.

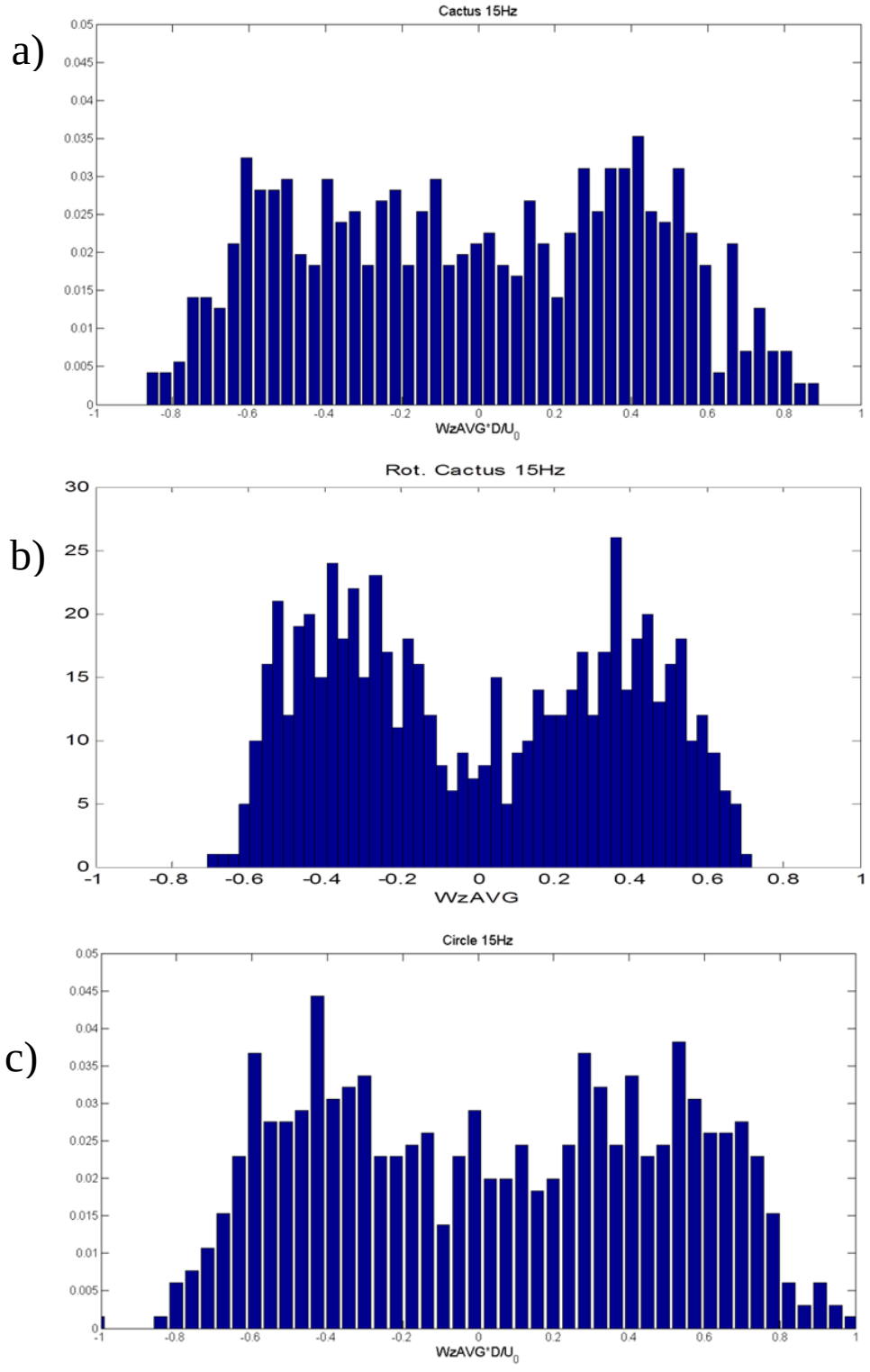

Figure 25: Histograms for spatially averaged vorticity $\omega/(U_0/D)$ fields at Re=50,000 for a) Cactus, b) Rotated Cactus, and c) Circular cylinder

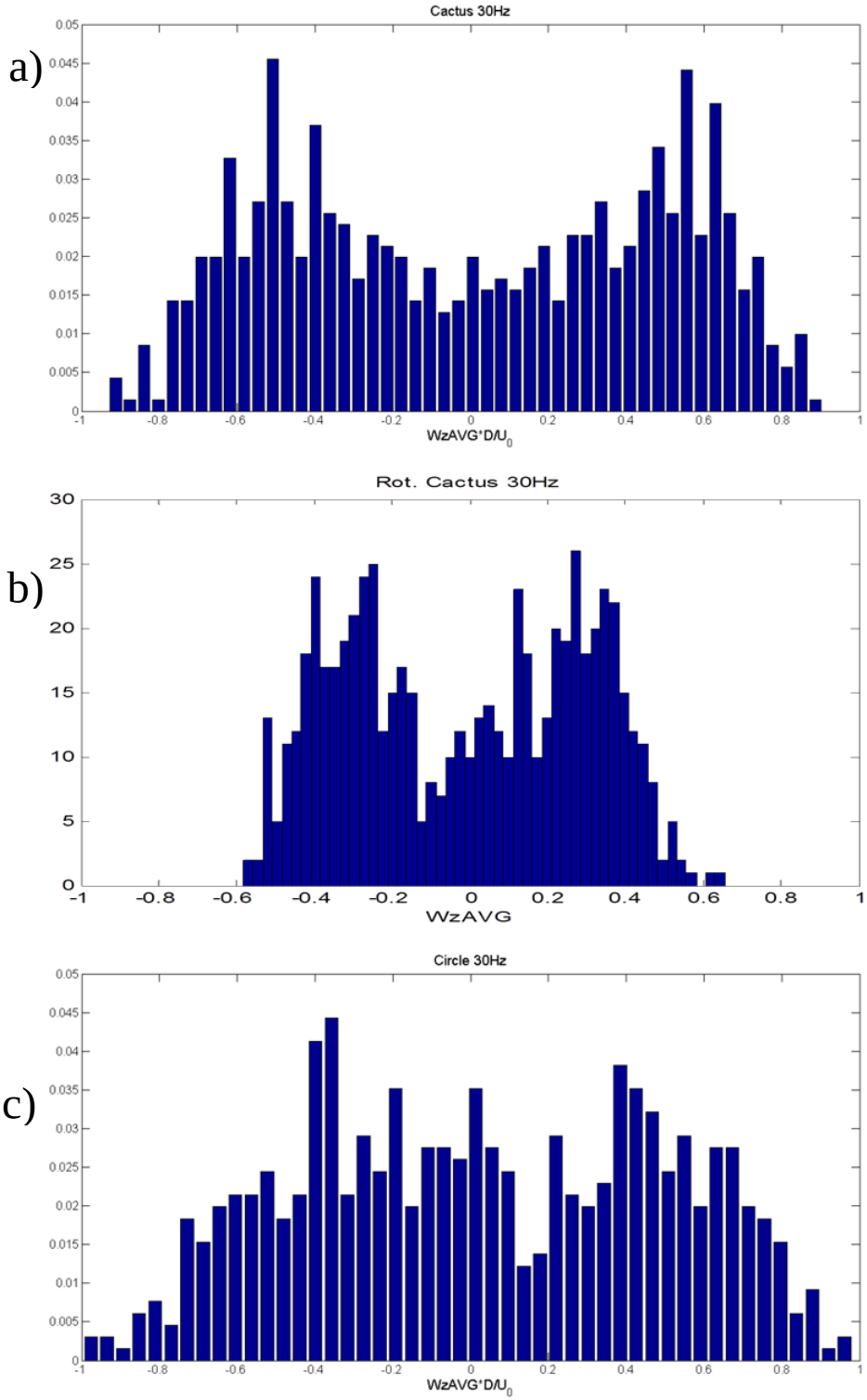

Figure 26: Histograms for spatially averaged vorticity $\omega/(U_0/D)$ fields at Re=110,000 for a) Cactus, b) Rotated Cactus, and c) Circular cylinder

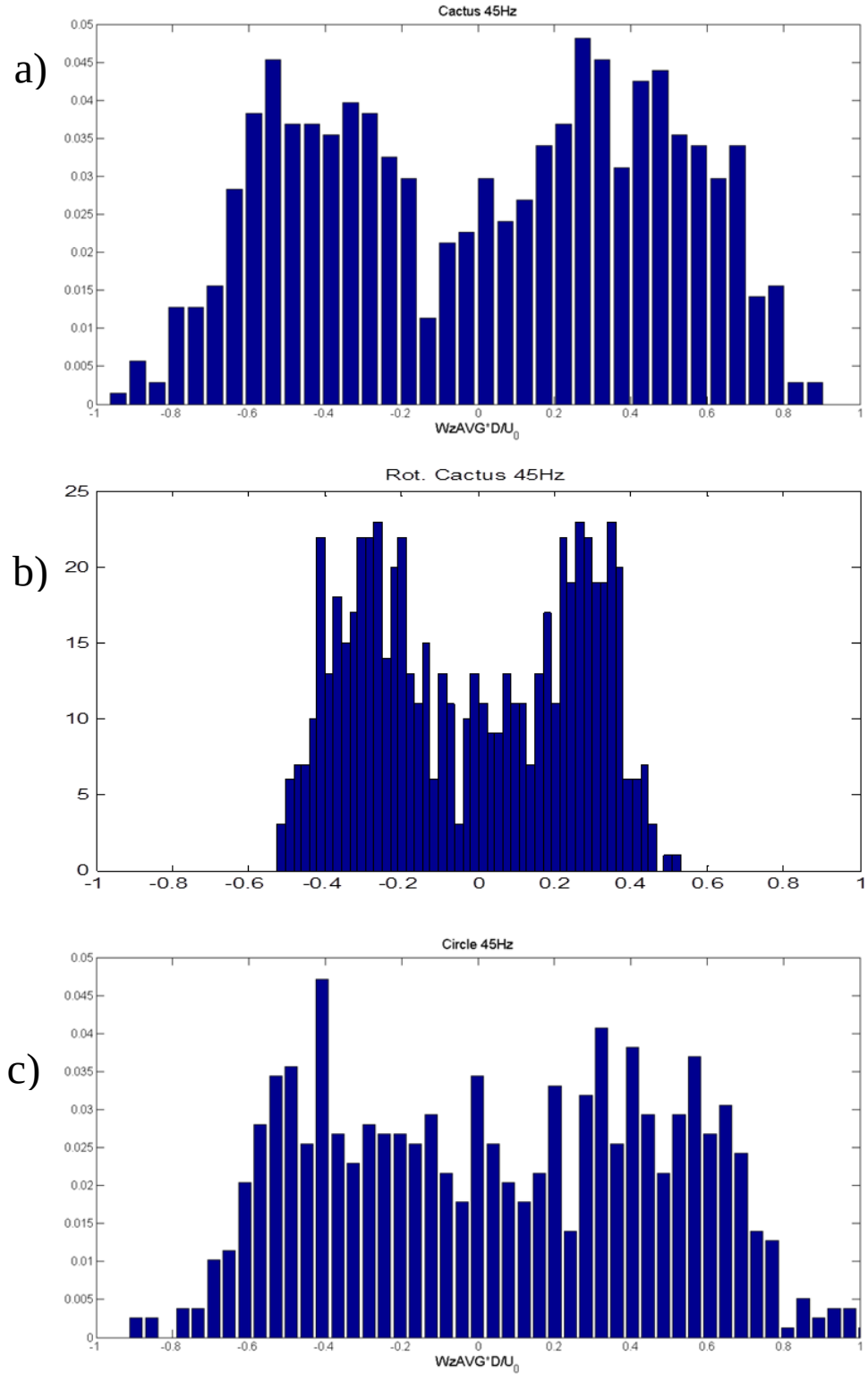

Figure 27: Histograms for spatially averaged $\omega/(U_0/D)$ vorticity fields at Re=170,000 for a) Cactus, b) Rotated Cactus, and c) Circular cylinder

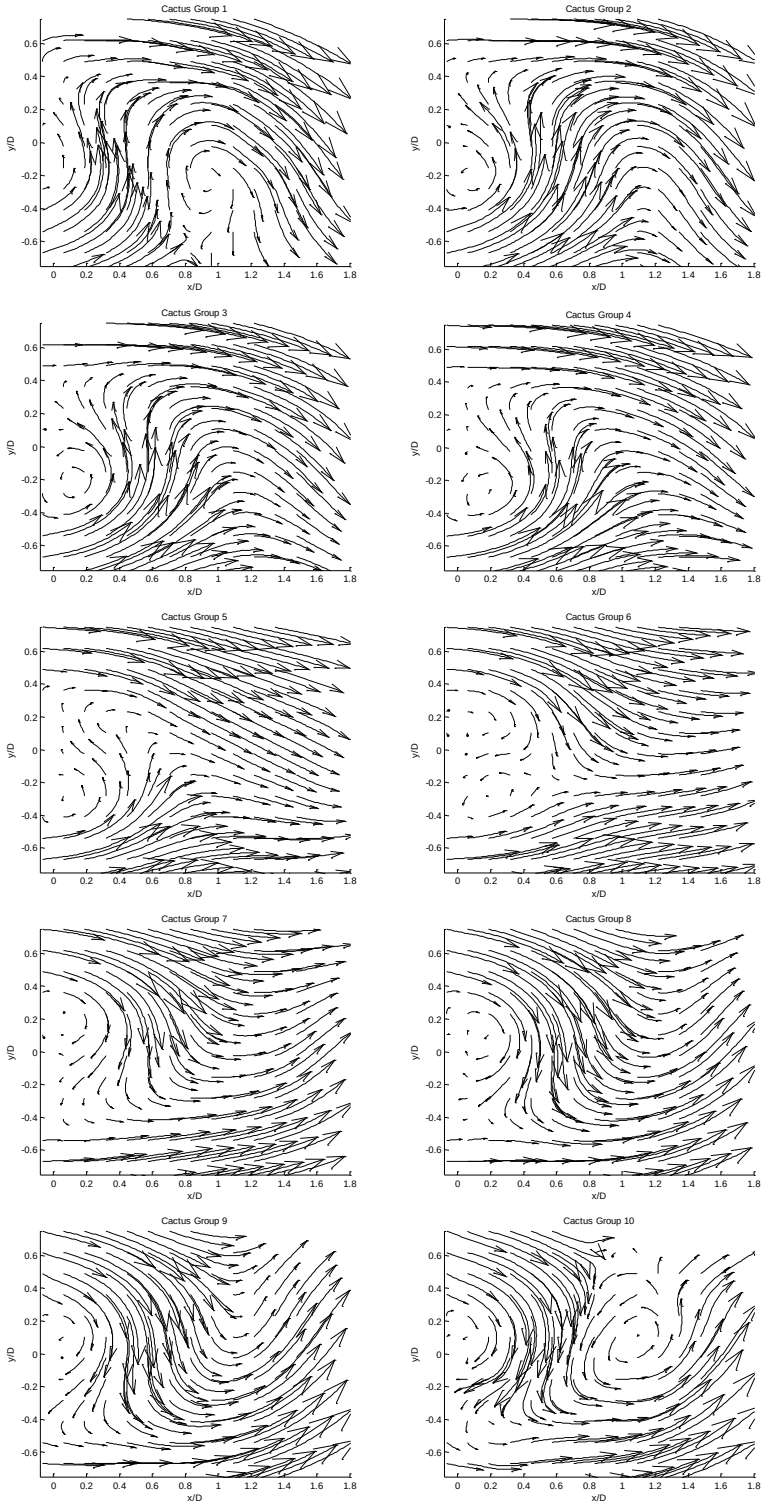

Figure 28: A posterior reconstruction of the temporal vortex shedding evolution in the cactus wake based on the histogram grouping method for Re = 170200. The vector fields are arranged left to right, top to bottom.

B. Surface Grooves Flow Analysis

The flow within the surface grooves was studied in order to explain the improved wake structure of the cactus compared to the circular cylinder. PIV was conducted for each lower groove separately, i.e. the field of view consisted only of one groove, and it was repeated four times to cover all lower grooves. The orientation of the cactus when the grooves were investigated is shown in Figure 4, and these grooves are labeled G1, G2, G3, and G4. Figure 28 shows the time averaged vorticity contours for the flow within the cactus lower grooves at Reynolds number of 110,000. The big arrow indicates the direction of the flow. In the first groove G1, a weak clockwise (CW) vorticity is generated by the upstream spike of the cactus, and it is convected near the surface inside G1. Moving downstream, this CW vorticity intensifies at the second spike where it sheds away in the outer layer of groove G2. A counter clockwise (CCW) is present near the surface of G2, while the CW vorticity is present in its outer layer. This suggests that the CCW vortices in G2 play an important role in attaching the boundary layer to the cactus surface causing consequently the delay of the separation of the boundary layer. When the CW vorticity is about to fade and weaken, it regain relatively its intensity at the third spike. This can be interpreted that the cactus spikes act as vortex generators that help in decreasing the shear force, delaying the boundary layer separation, and lubricating the flow around the cactus. In groove G3, the CW vorticity continues in the outer layer away from the surface, while weak CCW vorticity is present near the groove surface in a structure relatively similar to that of G2. This suggests increased unsteadiness and spatial meandering of the vorticity bands. The groove G4 is predominantly of CCW vorticity which is a sign of back flow and separation. The CCW vorticity intensifies at the spike between G3/G4.

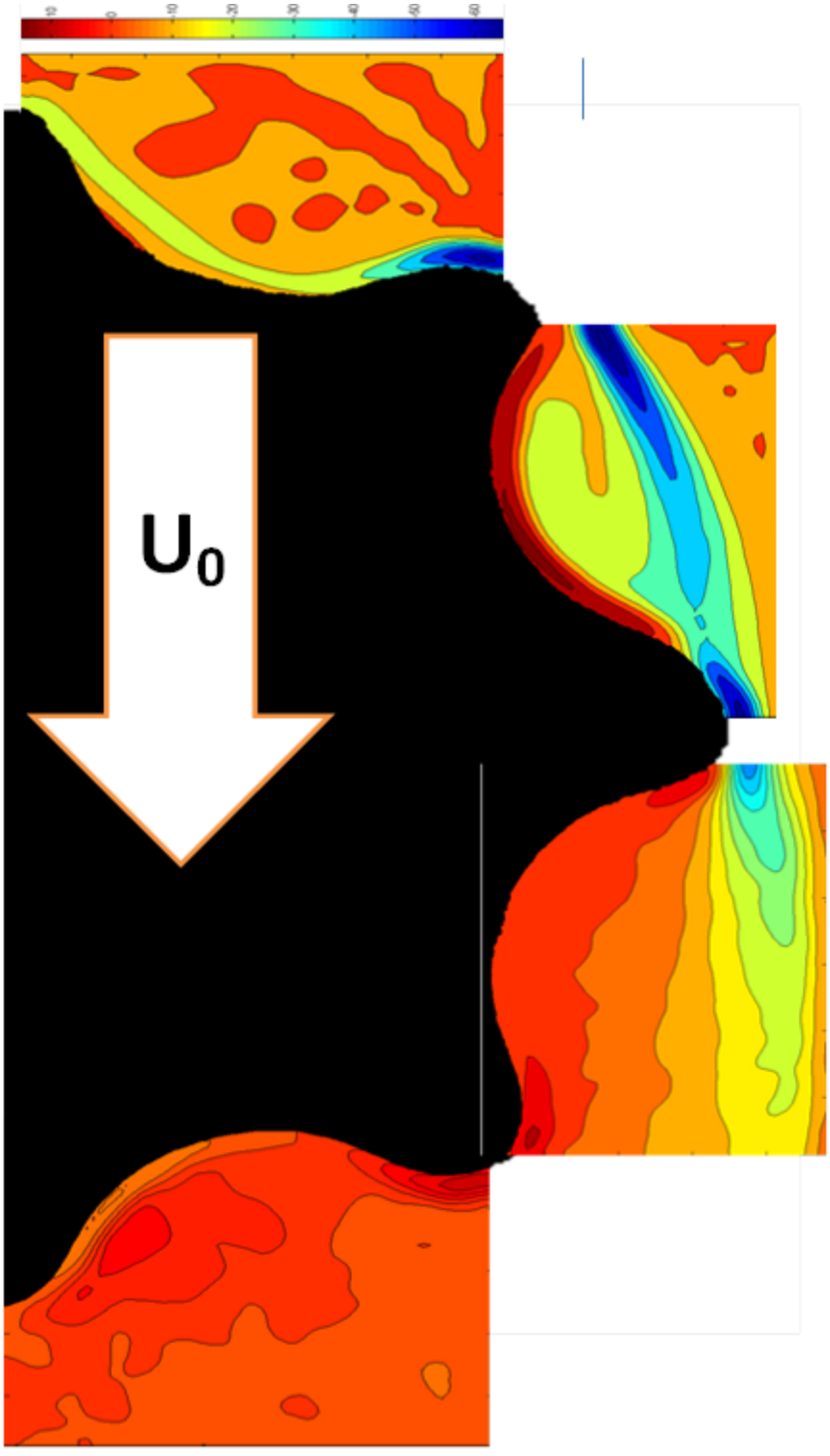

Figure 28: Temporal averaged vorticity $\omega/(U_0/D)$ contours of cactus lower grooves at Re=110,000

The vorticity peaks were identified for all instantaneous vorticity fields for all the lower cactus grooves. These peaks locations with respect to the cactus model are plotted in Figures 29 & 30. The blue circles and the red 'x' marks label the CW and CWW vortices, respectively. The markers' sizes are proportional to the vorticity peaks intensities. In groove G1, the instantaneous CW vortices are concentrated near the surface of the groove and they intensify in magnitude at the spike between G1 and G2. The cactus spike G1/G2 is a site for instantaneous vortex shedding. The CW vortices are then divided at that spike into two streams; the first one continues towards the spike G2/G3 in the outer layer of G2, while the other stream is convected inside G2 and interacts with CCW vortices along the entire surface of the groove. In groove G3, the CW and CCW vortices start wandering. Moreover, they start to wander aggressively at groove G4. This contributes to the fluctuating side forcing on the cactus. CCW vortices are noticed to exist in the interior side of G2 and G3. The CCW vortices when interact with CW vortices play an important role in attaching the boundary layer making steadier wake and smoother vortex shedding.

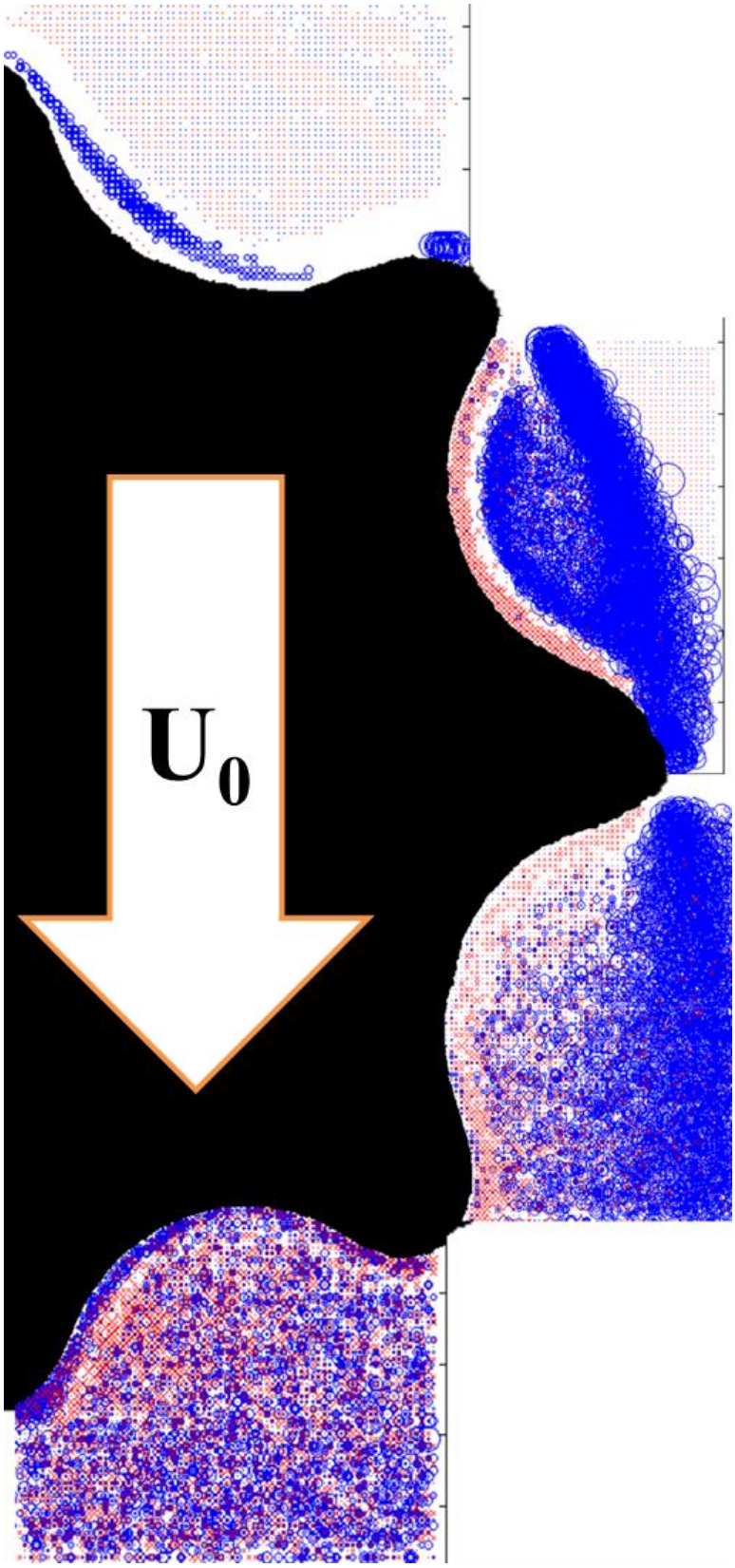

Figure 29: Scatter plot of the instantaneous positions of the identified vorticity peaks at Re=110,000

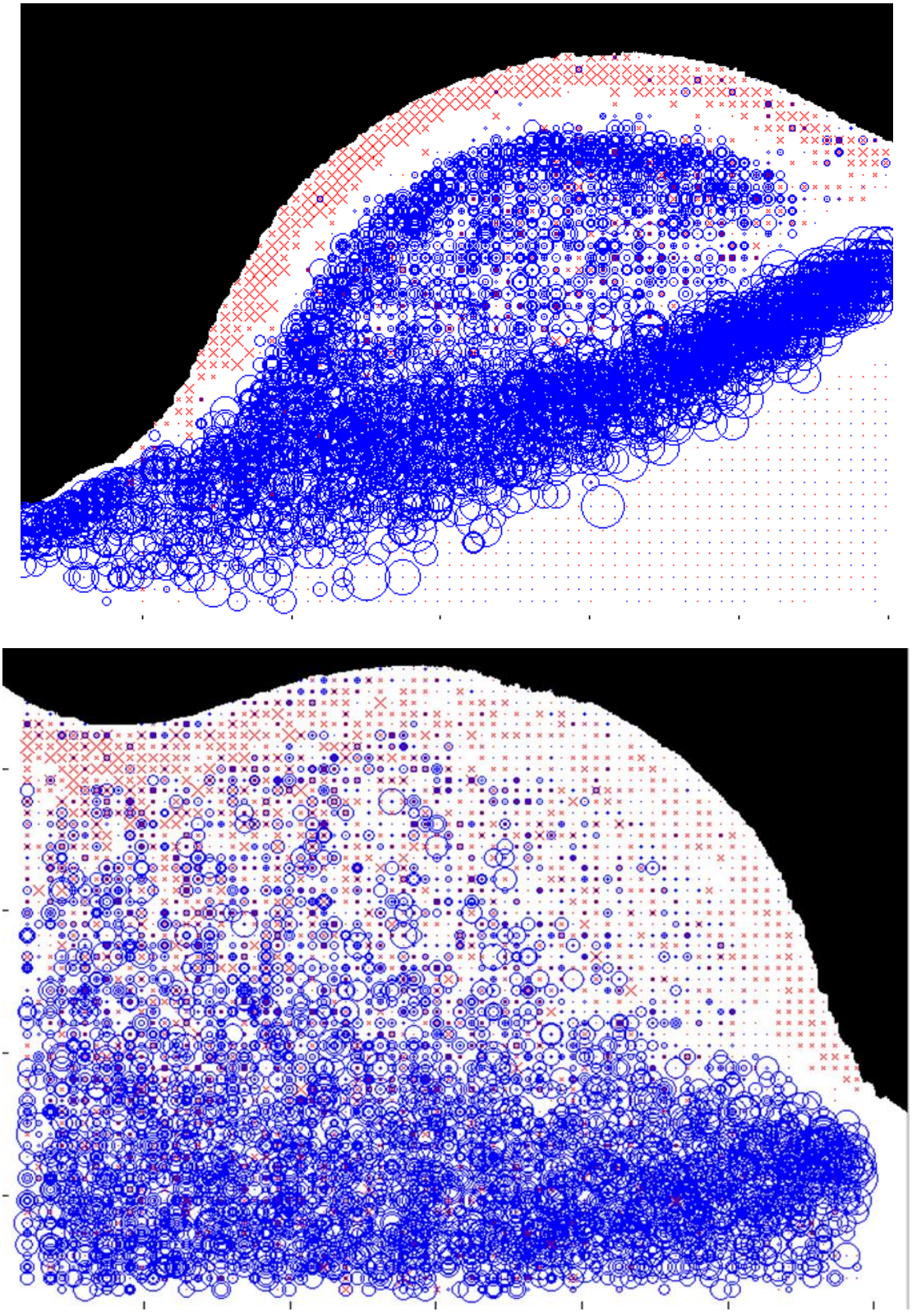

Figure 30: Zoomed Grooves 3 & 4

CHAPTER IV

ERROR ANALYSIS & MEASURMENT UNCERTAINTY

A. Bias Error

The bias error component is not easy to evaluate, but it can be inferred from comparison with other measurement methods. Although there have been numerous studies on the wake of a circular cylinder, there is a dearth of velocity measurements in the immediate wake at the Reynolds numbers considered here. We compare our data to the PIV measurements of Perrin et al. (2007) [33] and Djeridi et al. (2003) [34], and the hot wire data from Cantwell & Coles (1983) [35] – all for a circular cylinder at Re = 140,000. Figure 31 shows the streamwise turbulent velocity (u'^2/U_0^2) as a function of $\boldsymbol{y / D}$, for $x / D = 0.5$ at Re = 110,000 and 170,000 for the circular cylinder. The data from the current study agree more closely with the measurements of Perrin et al. (2007) and Djeridi et al. (2003) than with those of Cantwell and Coles (1983). Many factors contribute to these variations such as differences among studies in the type of testing facility, blockage and aspect ratios, spatial shifts of the shear layer location, and free stream turbulence levels. These factors render the estimation of the bias a challenging task. Nonetheless, since the PIV system (hardware/software) and test facility were used the same way to measure the circular and cactus cylinders flows, the level of measurement bias in the two geometrical models would be expected to be similar, and therefore, allowing the direct comparison between the two geometric models.

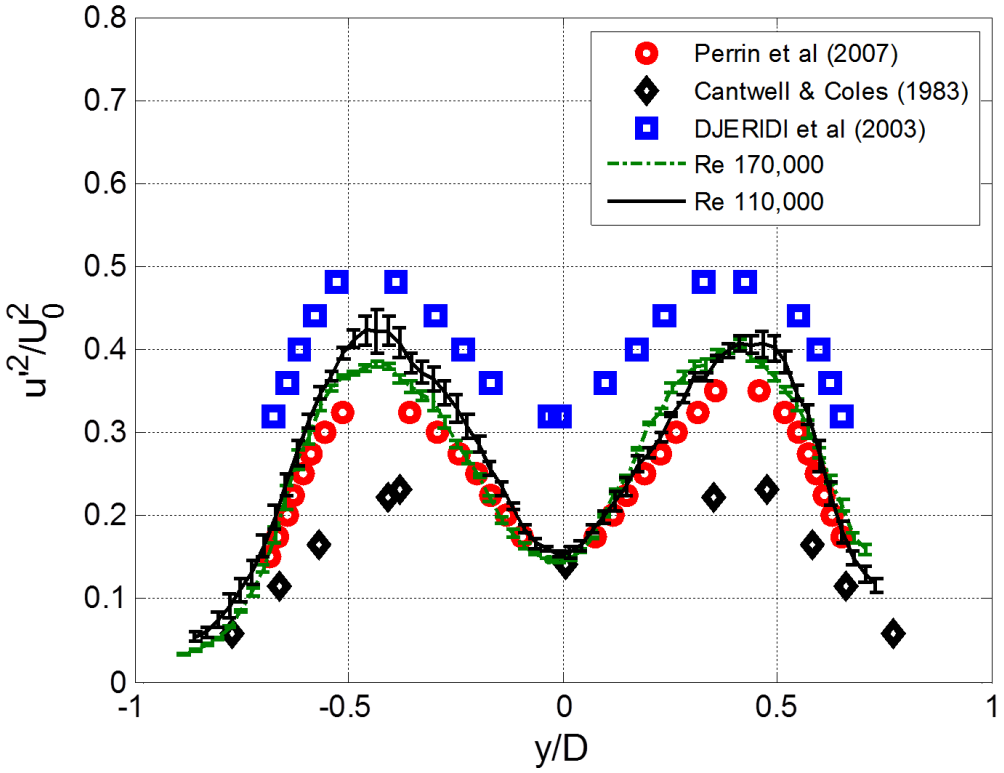

Figure 31: Streamwise turbulent velocity profile (u'^2/U_0^2) as a function of (y/D) for the circular cylinder at the downstream location ($x/D = 0.5$) at Re =110,000 and 170,000. The error bars mark the precision error to the 95% confidence level. Also shown are the PIV measurements of Perrin et al. (2007) and Djeridi et al. (2003), and the hotwire data of Cantwell and Coles (1983), all for a circular model at Re =140,000.

B. Precision Error

The precision error can be inferred from repeating the measurement multiple times, and computing the level of variability from the mean (e.g. standard deviation). To estimate the precision error, we divided the 650 vector fields into 7 independent batches of ~ 90 random vector fields. The turbulent velocities were computed for each of the independent batches; and the standard deviation of the means was estimated as outlined in Figliola & Beasley (2000) [36]. The bars in Figure 31 mark the precision error in (u'^2/U_0^2) to the 95% confidence level.

CHAPTER V

DRAG COEFFICIENT

Drag Coefficients were roughly computed for the test models at the three tested Reynolds numbers in order to give a rough idea about the effect of the improved wake structure on drag forces. Conservation of mass and momentum laws were applied in order to get the drag coefficient for each test case.

A. Control Volume and Mass Conservation

The control volume was chosen in a way where the mass flow rate is conserved i.e. the mass flow rate entering the control volume is equal to the exiting mass flow rate. Moreover, it is chosen outside the boundary layer of the test section walls and that of the test model in order to neglect the unkown shear and friction forces that are acted on the flow by the walls. The schematic of the control volume is shown in Figure 32.

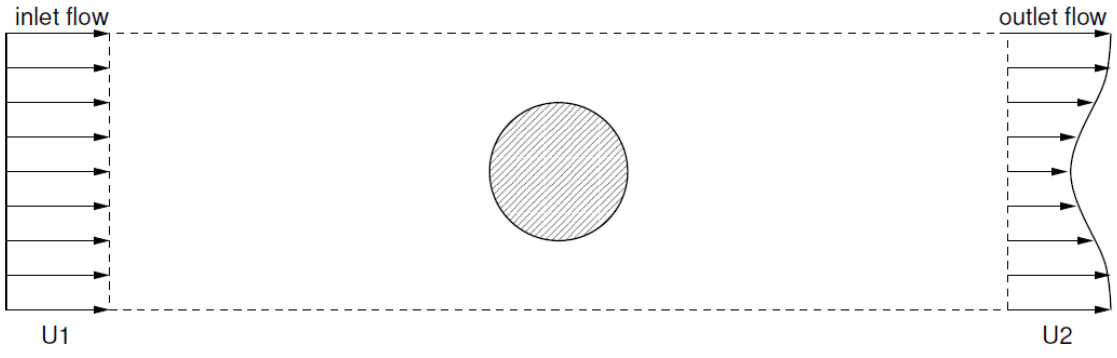

Figure 32: Control volume schematic

The mass flow rate across the control volume is conserved according to the following equation:

$$\int \rho U_1 dA_1 = \int \rho U_2 dA_2 \quad (2)$$

Where ρ is the density of the flowing air.

U_1 & U_2 are the inlet and outlet velocities, respectively.

A_1 & A_2 are the inlet and outlet surface areas of the control volume, respectively.

B. Momentum Conservation & Drag Coefficient

The general momentum conservation equation along the flow direction is:

$$Drag = \frac{d}{dt}\left(\int_{CV} U\rho dU\right) + \int_{CS} U\rho U dU \quad (3)$$

Since we are dealing with steady state flow, the transient term becomes zero. Therefore, the total drag acting on the test models were computed. Drag coefficients (C_D) were computed from drag forces using the following equation and they are listed in Table 2.

$$C_D = \frac{Drag}{{}^1/_2 \rho U_0^2 A} \quad (4)$$

Where U_0 is the upstream velocity

A is the projected area of the test model in the direction of the flow

Table 2: Drag Coefficient C_D

Test Model	Re = 50,000	Re = 110,000	Re = 170,000
Circular Cylinder	0.4955	0.4393	0.5127
Cactus Cylinder	0.4965	0.4648	0.4263
Rotated Cactus	0.4903	0.4675	0.4219

CHAPTER VI

CONCLUSION

Cactus plants are known for resisting the high wind storms in the dessert despite the fact that they have weak rooting systems. They have an aerodynamic superior behavior. In order to asses this superiority, PIV experiments were done on biologically inspired cactus model in a wind tunnel, and it was compared to similar model with circular cross section. Cactus exhibited improved wake behavior compared to its counterpart circular cylinder. The cactus wake is smaller and it is spatially closer to the cactus surface than the circular cylinder. Moreover, the cactus showed lower stream wise turbulent velocity for its both orientations. Therefore, the vortex shedding is smoother in the case of the cactus than the case of the circular cylinder. The temporal averaged vorticity contours showed that in the case of cactus the vortices structure is engulfing the model, while in the case of the circular cylinder, the vortices structure are elongated downstream the wake. The histograms of the instantaneously spatially averaged vorticity fields show two distinct peaks for the cactus model suggesting that the vortex shedding is more organized i.e. the upper and lower shear layers interact smoothly in a periodic way. A simple and crude method was used to group the instantaneous vector fields according to their spatially averaged vorticity fields. We were able to sort these vector fields and reconstruct the vortex shedding without the use of the cinematic PIV.

Moreover, PIV experiments were done on the flow within the lower cactus grooves in order to explain the improved wake behavior. It is shown that the spikes act

as vortex generators that help in attaching the boundary layer and consequently delaying its separation. CCW vortices are generated near the surface of grooves G2 and G3 which also play an important role in decreasing the shear friction and lubricate the flow.

The drag coefficients were computed for the test models at the three tested Reynolds numbers. The cactus and the circular cylinders have approximately the same drag coefficients.

REFERENCES

[1] Wu, Jie-ZhiMa; Hui-Yang; Zhou, Ming-De; Separated Vortex Flows; Vorticity and Vortex Dynamics; 2006; Springer Berlin Heidelberg; 978-3-540-29028-5; Engineering; 323:382

[2] Roshko A. 1955. On the wake and drag of bluff bodies. *J. Aeronaut. Sci.* 22:124–32

[3] Berger E,Wille R. 1972. Periodic flow phenomena. *Annu. Rev. Fluid Mech.*11:313-40

[4] Lin J, Pao Y. 1979.Wakes in stratified fluids. *Annu. Rev. Fluid Mech.* 11:317–38

[5] Bearman PW. 1984. Vortex shedding from oscillation bluff bodies. *Annu. Rev. Fluid Mech.* 16:195–222

[6] Oertel H. 1990.Wakes behind blunt bodies. *Annu. Rev. Fluid Mech.* 22:539–64

[7] Griffin OM, Hall MS. 1991. Review: vortex shedding lock-on and flow control in bluff body wakes. *Trans. ASME J. Fluids Eng.* 113:526–37

[8] Coutanceau M, Defaye J. 1991. Circular cylinder wake configurations: a flow visualization survey. *Appl. Mech. Rev.* 44:255–37

[9] Williamson CHK. 1996. Vortex dynamics in the cylinder wake. *Annu. Rev. Fluid Mech.* 28:477–539

[10] Williamson CHK. 2004. Vortex-induced vibrations. *Annu. Rev. Fluid Mech.* 36:413-55

[11] J. H. GERRARD (1961). An experimental investigation of the oscillating lift and drag of a circular cylinder shedding turbulent vortices.

[12] Bearman, P.W., Zdravkovich, M.M. (1977). Flow around a Circular Cylinder near a Plane Boundary. *Journal of Fluid Mechanics, 89 (pt 1), pp. 33-47*

[13] Baek S, Sung HJ. 1998. Numerical simulation of the flow behind a rotary oscillating circular cylinder. *Phys. Fluids* 10:869–76

[14] Choi S, Choi H, Kang S. 2002. Characteristics of flow over a rotationally oscillating cylinder at low Reynolds number. *Phys. Fluids* 14:2767–77

[15] Artana G, Sosa R, Moreau E, Touchard G. 2003. Control of the near-wake flow around a circular cylinder with electrohydrodynamic actuators. *Exp. Fluids* 35:580–88

[16] Kim S, Lee C. 2000. Investigation of the flow around a circular cylinder under the

influence of an electromagnetic force. *Exp. Fluids* 28:252–60

[17] Mutschke G, Gerbeth G, Shatrov V, Tomboulides A. 2001. The scenario of threedimensional instabilities of the cylinder wake in an external magnetic field: a linear stability analysis. *Phys. Fluids* 13:723–34

[18] Arcas D, Redekopp L. 2004. Aspects of wake vortex control through base blowing/ suction. *Phys. Fluids* 16:452–56

[19] Delaunay Y, Kaiktsis L. 2001. Control of circular cylinder wakes using base mass transpiration. *Phys. Fluids* 13:3285–302

[20] Leu TS, Ho CM. 2000. Control of global instability in a nonparallel near wake. *J. Fluid Mech.* 404:345–78

[21] Shih WCL, Wang C, Coles D, Roshko A. 1993. Experiments on flow past rough circular cylinders at large Reynolds numbers. *J.Wind Eng. Ind. Aerodyn.* 49:351–68

[22] Bearman PW, Harvey JK. 1993. Control of circular cylinder flow by the use of dimples. *AIAA J.* 31:1753–56

[23] Choi J, Jeon W-P, Choi H. 2006a. Mechanism of drag reduction by dimples on a sphere. *Phys. Fluids* 18:041702

[24] Lee S, Kim H. 1997. The effect of surface protrusions on the near wake of a circular cylinder. *J. Wind Eng. Ind. Aerodyn.* 69–71:351–61

[25] Anderson E, Szewczyk A. 1997. Effects of a splitter plate on the near wake of a circular cylinder in 2 and 3-dimensional flow configurations. *Exp. Fluids* 23:161–74

[26] Hwang J-Y, Yang K-S, Sun S-H. 2003. Reduction of flow-induced forces on a circular cylinder using a detached splitter plate. *Phys. Fluids* 15:2433–36

[27] Kwon K, Choi H. 1996. Control of laminar vortex shedding behind a circular cylinder using splitter plates. *Phys. Fluids* 8:479–86

[28] Ozono S. 1999. Flow control of vortex shedding by a short splitter plate asymmetrically arranged downstream of a cylinder. *Phys. Fluids* 11:2928–34

[29] Lim H, Lee S. 2002. Flow control of circular cylinders with longitudinal grooved surfaces. *AIAA J.* 10:2027–36

[30] Bushnell DM (1991) Drag reduction in nature. Ann. Rev. Fluid Mech., Vol 23, pp 65-79

[31] Abboud, J.E., Karaki, W.S., Oweis, G.F. (2011). Particle image velocimetry measurements in the wake of a cactus-shaped cylinder *Journal of Fluids Engineering, Transactions of the ASME, 133 (9), art. no. 094502*

[32] Raffel M, Wilbert C.E., Kompenhans, 1998 "*Particle image velocimetry: a practical guide*," Springer Verlag

[33] Perrin R., Cid E, Cazin S, Sevrain A, Braza M, Moradei F, Harran G (2007). Phaseaveraged measurements of the turbulence properties in the near wake of a circular cylinder at high Reynolds number by 2C-PIV and 3C-PIV," *Exp. In Fluids,*Vol **42**, pp 93-109

[34] Djeridi H, Braza M., Perrin R, Harran G, Cid E and Cazin S, (2003). Near-wake turbulence properties around a circular cylinder at high Reynolds number. *Flow Turb.& Combus.*, Vol. **71**, pp 19-34; DOI: 10.1023/B:APPL.0000014930.49408.53

[35] Cantwell B, and Coles D (1983). An experimental study of entrainment and transport in the turbulent near wake of a circular cylinder. *J. Fluid Mech*., Vol. **136**, pp 321-374

[36] Figliola RS, Beasley DE (2000). *Theory and design of mechanical measurements*. 3rd ed., Wiley, NY, pp 123-126. (ISBN 0471350834)